Renewable Energy 221 (2024) 119807

Contents lists available at ScienceDirect

Renewable Energy

journal homepage: www.elsevier.com/locate/renene

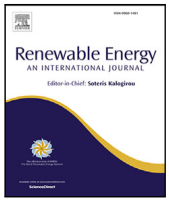

Comparison of the dynamic wake meandering model against large eddy simulation for horizontal and vertical steering of wind turbine wakes

Irene Rivera-Arreba [a,1], Zhaobin Li [b,1], Xiaolei Yang [b,*], Erin E. Bachynski-Polić [a,*]

[a] Department of Marine Technology, Norwegian University of Science and Technology, Trondheim, 7050, Norway
[b] Laboratory of Nonlinear Mechanics, Institute of Mechanics, Chinese Academy of Sciences, Beijing, 100190, PR China

ARTICLE INFO

Keywords:
Wind turbine wake
Dynamic wake meandering
Large eddy simulation
Wake deflection
Wake steering

ABSTRACT

Accurately predicting the evolution of wake is crucial for power output and structural load estimation in wind farms. This study aims to validate the dynamic wake meandering (DWM) model, an efficient mid-fidelity wake model, against large eddy simulation (LES). The predictive capabilities of the DWM model for various wake properties, namely time-averaged wake deficit, mean wake center deflection, amplitude, and frequency spectrum of wake meandering, are comprehensively analyzed using the IEA 15MW reference wind turbine under different yaw and tilt misalignment angles. Two turbulent inflows with varying shear and turbulence intensity levels are considered. The comparison highlights the significance of the filter size (C_{meand}) in DWM as a key parameter determining simultaneously the time-averaged wake deflection and meandering amplitude, with optimal values differing for horizontal and vertical wake displacements. When the appropriate C_{meand} values are selected, the implementation of the DWM model in FAST.Farm demonstrates good agreement with LES data, particularly concerning time-averaged wake deficit, wake centerline deflection, and wake meandering amplitude at eight rotor diameters downstream. However, the DWM model tends to overestimate the energy in the lower frequency region with Strouhal's number less than 0.1 and underestimate the wake oscillation induced by the shear-layer at higher frequencies, even though the wake motion standard deviation is accurately reproduced if the polar grid size is properly adjusted. Furthermore, the influence of the ground effect on downward wake deflection through tilt control is revealed. These findings clearly demonstrate the strengths and weaknesses of the current DWM model and can serve as a reference for the development of advanced wake models.

1. Introduction

The need to understand wake effects as a result of the interaction between wind turbines operating in the atmospheric boundary layer is of increasing importance, since they affect the overall performance of a wind farm. Wake effects imply power losses [1], which depend on several parameters such as turbulence intensity, turbine spacing, and atmospheric stability [2]. Measurements of a wind turbine completely in wake conditions may show up to 40% losses compared to a wind turbine operating in free flow [1,3]. Furthermore, wake effects cause an increase of fatigue loads for downstream wind turbines, especially for wind speeds below rated and with high turbulence intensity levels.

The main wake effects are deficit and meandering; additionally, the wake may experience a mean vertical or horizontal deflection. For onshore and offshore bottom-fixed wind turbines, the horizontal deflection of the wake is a consequence of the misalignment between the main direction of the incoming wind field and the rotor; the vertical deflection is a consequence of the built-in shaft tilt (referred to as *tilt* in the following) and vertical shear. For floating wind turbines, the platform pitch angle also contributes to the effective tilt angle, and thus to the vertical deflection [4–6]. Both the yaw misalignment and the tilted rotor, combined with the variation in the projected area of the rotor itself, affect the overall performance of the wind farm.

To reduce the negative effects of the wakes on the downstream wind turbines in a wind farm, several turbine control strategies have been developed and evaluated. A well-studied group of control strategies consists of wake steering, which changes the direction of wakes by deliberately misaligning the rotor and the wind. These strategies include yaw-based [7–10] and tilt-based control [8,11], which deflect the wake in the lateral and vertical directions, respectively. Understanding and predicting how these techniques impact the wake is essential for their implementation in utility-scale wind farms.

* Corresponding authors.
E-mail addresses: xyang@imech.ac.cn (X. Yang), erin.bachynski@ntnu.no (E.E. Bachynski-Polić).
[1] These two authors contributed equally.

https://doi.org/10.1016/j.renene.2023.119807
Received 8 July 2023; Received in revised form 5 December 2023; Accepted 11 December 2023
Available online 12 December 2023

Nomenclature

α	Shear exponent
α_c	Angle of attack
$\bar{y}_c$	Mean horizontal wake center position
$\bar{z}_c$	Mean vertical wake center position
β	Tilt angle
γ	Yaw angle
κ	Von Kármán constant
ν	Kinematic viscosity
ν_T	Eddy viscosity
ν_{amb}	Shear viscosity contribution
ν_{shear}	Ambient viscosity contribution
Ω	Rotational speed
ρ	Density
σ_u	Standard deviation of the longitudinal wind speed component
σ_v	Standard deviation of the lateral wind speed component
σ_w	Standard deviation of the vertical wind speed component
σ_{y_c}	Standard deviation of the lateral wake center position
σ_{z_c}	Standard deviation of the vertical wake center position
τ	Stress
τ_1	Time scale from Øye's dynamic inflow model.
D	Drag force
$\mathbf{e}_\mathrm{D}$	Drag unit vector
$\mathbf{e}_\mathrm{L}$	Lift unit vector
F	Aerodynamic force
f	Aerodynamic force per unit span
L	Lift force
u	Velocity vector in Cartesian coordinates
DWM	Dynamic wake meandering
LES	Large eddy simulation
θ	Deflection angle
$\widetilde{\Omega}$	Rotational wind speed dependent on the deflection angle
$\widetilde{C}_T$	Thrust coefficient normal to the rotor, dependent on the deflection angle
a_{avg}	Time-averaged induction factor
c	Chord length
C_D	Drag coefficient
C_L	Lift coefficient
C_meand	Parameter related to the polar grid diameter size in the DWM model
C_T	Thrust coefficient normal to the rotor for a non-yawed or non-tilted rotor
D	Rotor diameter
D_w	Wake diameter
f	Frequency
f_c	Cut-off frequency of the low-pass time-filter for the wake advection, meandering and deflection
F_{amb}	Ambient filter function to adjust the ambient viscosity contribution
F_{shear}	Shear filter function to adjust the ambient viscosity contribution
I_1	Inflow 1
I_2	Inflow 2
k_{amb}	Weight parameter for the ambient turbulence influence on the eddy-viscosity
k_{shear}	Weight parameter for the ambient turbulence influence on the eddy-viscosity
p	Pressure
P_{T2}	Power output of T2
P_{wake}	Available power in the wake
PSD	Power spectral density
r	Radial coordinate
R_N	Characteristic length scale
r_n	Radial distance of a point from the center of the wake plane
Re	Reynold's number
St	Strouhal's number
T	Thrust
t	Time
T_0	Thrust normal to the rotor plane when yaw and tilt angles are zero
T_1	Wind turbine in free wind
T_2	Wind turbine in the wake
TI	Turbulence intensity
TI_{amb}	Ambient turbulence intensity at the rotor
U	Streamwise component of the wind velocity
u^*	Friction velocity
U_N	Characteristic velocity
$U_{\infty,z_{HH}}$	Undisturbed streamwise incoming wind speed at hub-height
U_∞	Undisturbed incoming wind speed
U_n	Wind speed normal to the rotor plane
V	Lateral component of the wind velocity
V_r	Radial velocity component
V_x	Time-filtered disk average wind velocity normal to the actuator disk
V_{ref}	Relative flow velocity with respect to the rotating blade
W	Vertical component of the wind velocity
w_n	Spatial weighting factor to compute the disturbed wind velocity across a wake plane
y_c	Lateral position of the wake center
z_0	Surface roughness
z_{HH}	Hub height

The yaw-based wake control strategy has been a research focus of the wind energy and fluid mechanics community. Howland et al. [9] studied the wake deflection behind a yawed rotor by means of wind tunnel experiments and large eddy simulation (LES). In their study, the wind turbine was represented as a porous disk in uniform inflow. Bastankhah and Porté-Agel [7] also performed wind tunnel measurements, where they studied the characteristics of the wake of a yawed wind turbine by particle image velocimetry. They developed an analytical model to estimate the wake deflection and the far-wake velocity distribution for yawed turbines. Qian and Ishihara [12] proposed a new analytical wake model for a yawed turbine dependent on the thrust and turbulence intensity. Recently, the success of yaw control has been justified by a multi-month field measurement of a utility-scale wind farm, showing an evident increase of energy production [13].

The number of studies on the impact of vertical wake steering is small compared to the numerous studies on horizontal wake steering,

since implementing vertical wake steering is challenging for current bottom-fixed wind turbine designs. Research indicates that vertical steering of the wake also increases the power available to wind turbines downstream. Interestingly, the increase differs for cases with an upward and a downward deflection. Fleming et al. [14] studied the impact of tilting the rotor on two wind turbines inline, whereas Annoni et al. [15] did so for three turbines in a row. Both studies reported significant increase in the power output due to upward wake deflection. Johlas et al. [16] performed large eddy simulations of a 15 MW turbine for different rotor tilt angles to study the impact of downward wake steering on the wake geometry, shear and power production. Consistently with previous studies, they [16] found that due to the wake being tilted away, and replaced by higher wind speeds from above, the power available to a downwind rotor recovered faster. Nanos et al. [5] investigated the possibility of deflecting the wake behind a floating wind turbine downwards, by imposing a tilt angle by differential ballast control. Cossu [17,18] suggest that a negative tilt angle is not only able to mitigate the wake effect by steering the wake downwards, but it has the potential to increase the wind speed behind the wind turbine by creating high speed streaks in the atmospheric boundary layer.

Previous studies on wake steering are mainly based on high-fidelity large eddy simulation (LES), or wind-tunnel experiments. The dynamic wake meandering (DWM) model [19] is a mid-fidelity model which represents a compromise between accuracy and efficiency, and several works have aimed to validate it against high-fidelity LES, or experimental data. This model is based on the main hypothesis that wake meandering is driven by large-eddy structures in the atmosphere. However, there is a second mechanism which considers wake meandering as an intrinsic property of the wake. Both mechanisms have been confirmed to coexist at a utility-scale wind turbine wake, by computational simulations [20] and field measurements [21]. Churchfield et al. [22] compared DWM and LES with field data from the Egmond aan Zee offshore wind farm; the input turbulent wind field for the DWM model was based on a stochastic inflow turbulence generator, whereas for the LES model they used SOWFA, a high-fidelity simulator for the wind turbine dynamics and the fluid flow in a wind farm. Jonkman et al. [23] validated the DWM model, as implemented in FAST.Farm, a mid-fidelity tool developed at the National Renewable Energy Laboratory, against SOWFA (LES), for a series of yaw misalignment cases up to 15°, for a single row of three NREL 5 MW turbines separated by eight rotor diameters. In this work, they showed a good agreement between the statistical distribution of the horizontal and vertical wake meandering against LES, suggesting that the DWM model is a very promising compromise between accuracy and efficiency. However, previous studies investigated neither how the DWM model performs when considering wake steering at larger yaw angles, for tilt steering in the vertical direction, and for larger wind turbines, nor the consequence of not accounting for the shear layer instability wake meandering mechanism.

For this reason, the objective of the current research is to validate the DWM model, a computationally more efficient model compared to large eddy simulations, focusing on its ability to predict wake evolution under various horizontal and vertical wake steering strategies. The research fills the knowledge gap on whether the DWM model, based on a large eddy mechanism to model the wake meandering phenomenon, can accurately capture both the average wake deflection resulting from both horizontal and vertical wake steering techniques (yaw or tilt) and the instantaneous oscillations (meandering). The focus is on the model predictive capability of the mean wake deficit, wake center deflection, wake meandering statistics and frequency characteristics. To achieve this, the wake of IEA 15 MW wind turbine [24] is predicted by both DWM and LES and is systematically compared. The analyses in the current work comprise twenty different cases, including 2 inflows with different shear and turbulence intensities, each of them for 10 different wind turbine misalignment angles (4 yaw, 5 tilt and 1 baseline). Finally, the comparison is conducted to determine the model applicability in predicting both the mean and dynamic wake effects under wake steering techniques, as well as to identify any limitations that may require future development.

The remainder of the paper is structured as follows. Section 2 describes the two methods compared throughout this work: LES by VFS-Wind and the DWM model as implemented in FAST.Farm. Section 3 gives an overview of the simulation set-up, the wind turbine model, the generation of the wind field and the characteristics of the computational domain in VFS and FAST.Farm. Section 4 analyses the time-averaged deficit and wake meandering statistics of the DWM model with respect to the LES data. The main limitation of the employed DWM model is discussed in Section 5. The DWM is applied to investigate the effect of horizontal and vertical wake steering techniques on a waked wind turbine in Section 6. The conclusions on this work are retrieved in Section 7.

2. Methodology

2.1. Large eddy simulation

We employ the large eddy simulation code of the Virtual Flow Simulator [25] to provide high-fidelity turbulent flow simulations. The wind version of the code employed in this study, VFS-Wind [26], provides extra functionalities for wind energy applications and has been widely applied to reveal the fluid mechanics of wind turbine wake [27–29], and to investigate complex flow in large-scale wind farms [30–32].

The solver treats the airflow as a Newtonian fluid with a constant density and viscosity. The governing equation is the filtered incompressible Navier–Stokes equation, as follows:

$$\nabla \cdot \widetilde{\mathbf{u}} = 0, \tag{1}$$

$$\frac{\partial \widetilde{\mathbf{u}}}{\partial t} + (\widetilde{\mathbf{u}} \cdot \nabla)\widetilde{\mathbf{u}} = -\frac{1}{\rho}\nabla \widetilde{p} + \nu \nabla^2 \widetilde{\mathbf{u}} - \nabla \cdot \boldsymbol{\tau} + \frac{\mathbf{f}}{\rho}, \tag{2}$$

where $\mathbf{u} = \{u, v, w\}$ is the velocity vector in the Cartesian coordinates, p is the pressure, ρ is the fluid density, and ν is the fluid kinematic viscosity. $\widetilde{\cdot}$ denotes the spatial filtering, and $\boldsymbol{\tau}$ is the subgrid-scale stress and is closed with the eddy-viscosity model [33]. $\mathbf{f}$ is a body force term employed to represent the effect of wind turbines on the flow and is computed using a well-validated actuator surface model [34], described in Section 3.2.

The governing equations are discretized using the finite differencing method on a structured rectangular grid. The spatial discretization uses the second-order central differencing scheme. The temporal integration employs a second-order fractional step scheme. The nonlinear momentum equation is solved by the Jacobian-free Newton–Krylov approach [35]. The Poisson equation, derived from the continuity equation to enforce incompressibility, is solved by the Generalized Minimal Residual (GMRES) approach [36] with multigrid as a preconditioner. The reader can refer to Ge and Sotiropoulos [37] for a detailed description of the implementation of the above numerical approach with a staggered structured grid.

Large eddy simulations, in conjunction with actuator-type wind turbine parameterization, have been widely adopted to predict the turbulent wake of wind turbines, as comprehensively reviewed by Li et al. [38] for their theoretical foundations, numerical implementation, and predictive capabilities. The advantage of employing actuator models is the balance between computational efficiency and accuracy. These models enable the LES code to concentrate on resolving the large-scale turbulent wake motion, spanning several kilometers, while avoiding the computationally intensive task of resolving the boundary layer aerodynamics of rotor blades at the centimeter scale. In the literature, several actuator-type models have been proposed for LES wake simulations, including the actuator disk [39], actuator line [40], actuator surface (AS) [34,41], listed in increasing order of complexity. Existing research has generally concluded that employing actuator models exhibits robust predictive capabilities for the far wake, particularly when accounting

for inflow turbulence in the simulations [34,42,43]. For cases with laminar inflow conditions, it has been found that the simulation results can be sensitive to wind turbine parameterization [44,45] and predicting the tip vortex in the near-wake can be challenging [46,47]. Since the present study focuses on the wake meandering phenomenon, i.e., the large-scale motion in the far wake under turbulent inflow, we consider the LES-AS method a sound approach for generating the wake data. Furthermore, the predictive capability of VFS-Wind has been systematically validated. For utility-scale wind turbines with a diameter of 96 m and a Reynolds number of approximately 6.4×10^7, VFS-Wind has shown its ability to replicate the complex flow features observed in the near-wake, including intricate tip vortices, using super-large-scale particle image velocimetry [48,49]. The code's capability to replicate the wake deflection and deformation resulting from wind turbine yaw control has also been demonstrated with the 96 m wind turbine [28]. Even though a wind turbine with a diameter of 240 m and Reynolds number of approximately 1.6×10^8 is used in this study, VFS-Wind is still considered a valid method because the flow mechanism that drives the wake evolution is found to be independent of the Reynolds number within the range of $Re > 9.3 \times 10^4$ [50].

2.2. Dynamic wake meandering model in FAST.Farm

The basis behind the mid-fidelity dynamic wake meandering (DWM) model is the division of turbulence scales by a *cut-off eddy size* filter: turbulent eddies smaller than this size affect the evolution of the wake deficit, whereas the larger eddies mainly impact wake meandering. This size can be a model parameter, but it is usually taken to be two rotor diameters. The original model as proposed by Larsen et al. [19] consists of three submodels: the wake deficit, the wake meandering and the added-wake turbulence. The wake deficit evolution is described in the meandering frame of reference, and is modeled by the thin shear-layer approximation of the Reynolds–averaged Navier–Stokes equations under quasi-steady-state conditions in axisymmetric coordinates, in the far-wake region, as:

$$U\frac{\partial U}{\partial x} + V_r\frac{\partial U}{\partial r} = \frac{\nu_T}{r}\frac{\partial}{\partial r}\left(r\frac{\partial U}{\partial r}\right), \tag{3}$$

where U is the axial velocity component, V_r the radial velocity component, r the radial coordinate and ν_T the eddy viscosity. The turbulence closure is modeled by an eddy-viscosity formulation, which assumes that the velocity gradients are higher in the radial direction as compared to those in the axial direction; the pressure term is neglected.

FAST.Farm [51] is a multiphysics engineering tool used to predict the power performance and structural loads of wind turbines within a wind farm. This software uses OpenFAST version 3.4.0 [52], to solve the aero-hydro-servo-elastic dynamics of each individual turbine, and is based on the implementation of the DWM to account for wake deficit and meandering. The eddy-viscosity is modeled by the longitudinal distance x-dependent filter parameters F_{amb} and F_{shear}, which were described and calibrated by Madsen et al. [53], and extended by Larsen et al. [19] and Keck [54]. The eddy-viscosity $\nu_T(x,r)$, dependent on x and the radial position r, can be divided into the ambient viscosity and the shear viscosity contributions, $\nu_{amb}(x)$ and $\nu_{shear}(x,r)$, respectively, as:

$$\begin{aligned}\nu_T(x,r) &= \nu_{amb}(x) + \nu_{shear}(x,r)\\ &= F_{amb}(x)k_{amb}TI_{amb}V_x\frac{D_w}{2}\\ &+ F_{shear}(x)k_{shear}\max\left\{\left(\frac{D_w}{2}\right)^2\left|\frac{\partial V_x}{\partial r}\right|, \frac{D_w}{2}V_{x,min}\right\},\end{aligned} \tag{4}$$

where k_{amb} and k_{shear} are weight parameters for the ambient and shear turbulence influence on the eddy-viscosity, V_x is the time-filtered disk average wind velocity normal to the actuator disk, TI_{amb} is the ambient turbulence intensity at each rotor, and D_w is the wake diameter, which in this work is set to be equal to the rotor diameter D. The filter functions F_{amb} and F_{shear} depend on user-specified calibrated parameters. The parameters used in this research are based on the work of Doubrawa et al. [55].

FAST.Farm allows for both a polar and a curl formulation for the wake. The former implies that the wake, which is defined on a polar grid, is axisymmetric, and it is solved using an implicit Crank–Nicolson scheme, which satisfies both the momentum and mass conservation laws under a shear-layer approximation. In the latter, the wake is defined on a Cartesian grid and, and even though the effect of skewed inflow is accounted for by introducing cross-flow velocities, a first-order forward scheme is applied. In this work, despite the fact that the effect of curled wake vortices in skewed inflow is not captured, the polar formulation is applied, given the higher robustness. The radial increment of the radial finite-difference grid is set to 5 m and the cut-off frequency of the low-pass time-filter f_c for the wake advection, deflection, and meandering model is 0.1 Hz, based on Branlard et al. [56]. They define the filter frequency f_c in terms of the time scale τ_1 used in Øye's dynamic inflow model [57], as:

$$f_c = \frac{2.4}{\tau_1} \quad \text{with} \quad \tau_1 = \frac{1.1 \cdot D}{2U_{\infty,z_{HH}} \cdot (1 - 1.3\min(a_{avg}, 0.5))}, \tag{5}$$

where a_{avg} is the time-averaged induction factor and $U_{\infty,z_{HH}}$ the streamwise incoming undisturbed wind speed at hub-height (HH), z_{HH}. The remaining parameters, namely the calibrated parameters related to the near-wake correction, to the eddy-viscosity filter and to the wake diameter calculation, respectively, are set to the default values. The advection, deflection, and meandering velocity of each wake plane for each turbine is calculated as the weighted spatial average of the disturbed wind velocity on the wake plane. Larsen et al. [19] proposed a uniform spatial average where every point within a circle diameter of $2D_w$ weigh the same. In FAST.Farm, an alternative is to use a weighting parameter which weighs each point in the spatial average by a form of a jinc function dependent on the radius of the point from the wake centerline, r_n, and is normalized by $C_{\text{meand}}D_w$, which results in a weighting parameter computed as:

$$w_n = \text{jinc}\left(\frac{r_n}{C_{\text{meand}}D_w}\right)\text{jinc}\left(\frac{r_n}{2C_{\text{meand}}D_w}\right). \tag{6}$$

This method yields an improved low-pass filter with a cut-off wave number of $\frac{1}{C_{\text{meand}}D_w}$. The characteristic cut-off wave number proposed by Larsen et al. [19], equal to $\frac{1}{2D_w}$, can be applied by setting $C_{\text{meand}} = 2$. In other words, C_{meand} determines the size of the polar grid used to calculate the spatial-averaged velocity that is used to meander the wake deficits. Therefore its value impacts the amount of wake deflection that occurs. Discussion on the choice of the filter size for the cases without rotor misalignment and wake deflection exists in the literature. For example, Cheng and Porté-Agel [58] proposed a low-pass-filter threshold proportional to the time delay due to downstream advection based on Taylor's diffusion theory, and therefore if the location of interest for predicting the wake is on the downstream distance x, the temporal filter should have a size of $\frac{x}{U_{\infty,z_{HH}}\alpha}$, with $\alpha = 3$. Brugger et al. [59] found that, based on field measurements at a utility-scale wind turbine, this filter gave similar results to the one proposed by Larsen et al. up to $6D$ downstream, but the correlation between the wake meandering and the v-component by using this filter improved further downstream. In this work, the value for C_{meand} is chosen based on the best fit to the mean and standard deviation of the vertical and horizontal wake deflection resulting from the LES data, and the impact of this parameter on the wake meandering is discussed in Section 5.2.

3. Numerical set-up

3.1. Simulation set-up

We compare the predictive capability of the DWM model and LES in 20 different scenarios, namely 10 different yaw/tilt angles (four yaw

Table 1
Simulation cases for the two scenarios of yaw misalignment (*Yaw*) and tilt deflection (*Tilt*).

Case	0	1a	2a	3a	4a	1b	2b	3b	4b	5
Yaw	$\beta = 0°$	$\gamma = 10°$	$\gamma = 15°$	$\gamma = 20°$	$\gamma = 30°$	$\gamma = 0°$	$\gamma = 0°$	$\gamma = 0°$	$\gamma = 0°$	$\gamma = 0°$
Tilt	$\gamma = 0°$	$\beta = 0°$	$\beta = 0°$	$\beta = 0°$	$\beta = 0°$	β = -6°	$\beta = 6°$	$\beta = 10°$	$\beta = 15°$	$\beta = 20°$

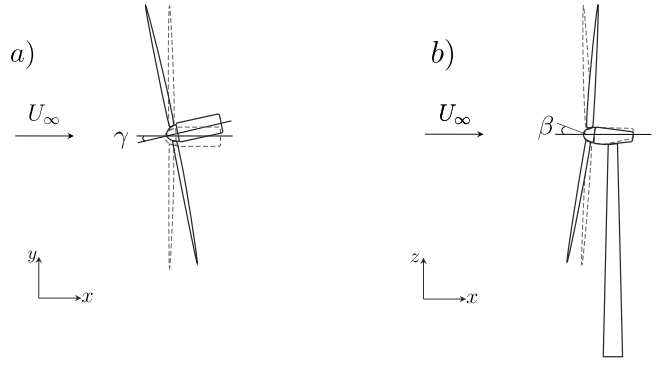

Fig. 1. (a) Top-view of the yawed rotor with a positive yaw misalignment angle indicated as γ. (b) Side-view of the tilted rotor with the positive tilt angle indicated as β. U_∞ is the incoming undisturbed wind speed.

Table 2
Fitted C_{meand} filter values based on the results at $x = 8D$ downstream, for both incoming inflows.

Case	1a	2a	3a	4a	1b	2b	3b	4b	5
C_{meand}	1.90	2.00	2.00	2.10	2.90	2.90	3.22	3.25	3.50

angles γ, and five tilt angles β, and one case with $\gamma = \beta = 0$), and each of them for two turbulent inflow conditions. A positive yaw misalignment angle γ and a positive tilt angle β are depicted in Fig. 1. Table 1 presents the yaw misalignment angle and the tilt angle for every simulated case. For every case in Table 1, the C_{meand}, or polar grid size, that yields the closest mean and standard deviation of the wake mean deflection and standard deviation compared to LES, measured at $8D$ downstream, is provided in Table 2. For the cases with yaw misalignment (1a to 4a) the mean value of this filter is 2.0, and for the cases with tilt deflection (1b to 5), 3.2. For the case with no yaw misalignment or tilt deflection angle (case 0), C_{meand} is set based on Cheng and Porté-Agel [58], which yields a higher value than the default one proposed by Jonkman and Shaler [51] and Larsen et al. [19]. The effect of using a different filter C_{meand} is analyzed in Section 5.2.

3.2. Wind turbine model set-up

The IEA 15 MW reference wind turbine [24], with a rotor diameter of 240 m and 150 m hub-height, is used. Since the focus of this research is on validating the DWM against LES, the turbine rotor model and operational parameters were defined as similarly as possible in both models. To this end, for both methods, we use a simple control strategy with a constant tip speed ratio $\widetilde{\lambda} = \Omega D/(2U_n)$, defined with respect to the wind speed normal to the rotor $U_n = U_{\infty,z_{HH}} \cos\theta$, with $U_{\infty,z_{HH}}$ being the streamwise velocity at hub-height. The rotational speed dependent on θ is defined as $\Omega = \widetilde{\Omega}\cos\theta$, where θ is used indistinctly here for yaw or tilt angles. $\widetilde{\Omega} = 6.4$ rpm represents the rotational speed for the case without yaw and tilt. We note that this simple strategy is only to keep the velocity triangle experienced by the rotor blades similar for cases with different misalignment angles (θ) and may not represent the optimal control strategy under yaw and tilt misalignment.

In VFS, the aerodynamics of the wind turbine rotor were computed using the actuator surface (AS) model proposed by Yang and Sotiropoulos [20]. This model simplifies the rotor blades as zero-thickness force-carrying surfaces. The aerodynamic forces are computed along the blade using two-dimensional airfoil coefficients, as follows:

$$\mathbf{f} = \mathbf{F}/c = (\mathbf{L} + \mathbf{D})/c, \tag{7}$$

$$\mathbf{L} = \frac{1}{2} c\rho C_{\text{L}}(\alpha_c, Re)|V_{\text{ref}}|^2 \mathbf{e}_{\text{L}} \tag{8}$$

$$\mathbf{D} = \frac{1}{2} c\rho C_{\text{D}}(\alpha_c, Re)|V_{\text{ref}}|^2 \mathbf{e}_{\text{D}}, \tag{9}$$

where $\mathbf{f}$ is the aerodynamic force $\mathbf{F}$ per unit span, with $\mathbf{L}$ and $\mathbf{D}$ the lift and drag, and $C_{\text{L}}(\alpha, Re)$ and $C_{\text{D}}(\alpha, Re)$ the lift and drag coefficients, depending on the local airfoil and the angle of attack (α_c) and the Reynolds number (Re) defined with the chord length (c). V_{ref} is the relative flow velocity with respect to the rotating blade, $\mathbf{e}_{\text{L}}$ and $\mathbf{e}_{\text{D}}$ are unit vectors defining the lift and drag directions. 3D effects [60] and tip losses [61] are corrected before computing the momentum source in Eq. (2).

In OpenFAST, the loads on the rotor are computed based on the blade-element/momentum (BEM) theory by Glauert [62]. To reduce the sources of uncertainty when comparing the wake deflection between LES and the DWM model, the wind turbine parameters in OpenFAST are set so that the rotor angular speed $\widetilde{\Omega}$ is fixed to the same value as for the actuator surface in VFS. Additionally, the blades in both approaches are modeled as rigid.

To verify the similarity of the set-up of the wind turbine in both models, Fig. 2 compares the thrust T of the rotor for the two models as a function of yaw and tilt angles (γ and β, respectively). The thrust is defined as normal to the rotor plane for every case shown here. The values are normalized by T_0, which corresponds to the thrust normal to the rotor plane when the yaw misalignment or the tilt angle is zero. Given the control strategy in the current study, the thrust follows closely the relation $\cos^2\theta$, with $\theta = \gamma$ or β, in the two models and for every tilt or yaw angle case, which is consistent with previous findings [63–65]. The thrust coefficient $\widetilde{C_T}$ and the rotational speed $\widetilde{\Omega}$ for zero tilt and yaw angles are presented in Table 3.

Table 3
Thrust coefficient $\widetilde{C}_T$ and rotational speed $\widetilde{\Omega}$ for the case without yaw and tilt.

$\widetilde{C}_T$	$\widetilde{\Omega}$
0.78	6.4 rpm

3.3. Turbulent inflow wind generation and characteristics

For every case presented in Table 1, the turbine is subjected to two incoming turbulent wind fields. The incoming wind fields are generated by large eddy simulations, with a half-channel configuration with periodic boundary conditions to mimic fully developed atmospheric boundary layer flow. The ground roughness length z_0 is employed to control the wind profile and the turbulence intensity level [66]. The precursory LES employed a large computational domain to capture large-scale turbulent structures in the atmospheric boundary layer [67, 68], which measures approximately 22.5 km × 15 km × 1 km in the lateral, streamwise, and vertical directions. The streamwise and spanwise grid intervals are $\Delta x = 20$ m and $\Delta y = 10$ m, respectively. In the vertical direction, the grid is refined towards the ground and has a grid size of approximately $\Delta z \approx 2$ m in the first layer. The present resolution results in a total number of grid points equal to 254 million. The time step for the simulation is $\Delta t = 1$ s. In the precursory simulations, instantaneous velocity fields on a plane perpendicular to the mean flow direction are saved each time step and applied as inflow

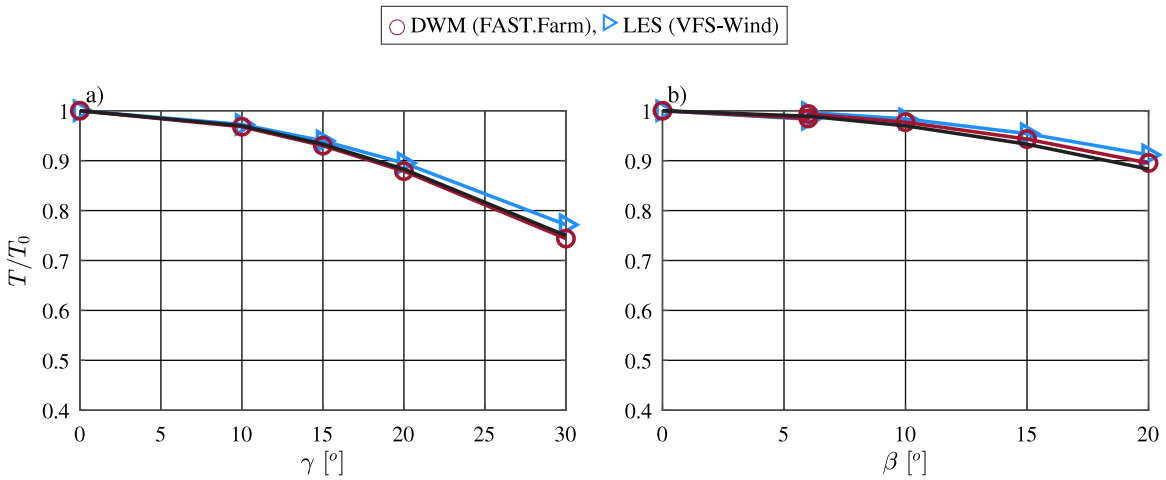

Fig. 2. Thrust as a function of the yaw (γ) and tilt (β) angles, normalized by T_0: (a) for the yaw misalignment angle cases, and (b) for the tilt angle cases. The black solid line represents the $\cos^2\theta$ relation, with $\theta = \gamma$ or β.

conditions for the turbine wake simulations in the LES and DWM models. To use the wind fields generated by LES directly as input to the DWM model, these were converted to a supported format. Prior to converting them, they were linearly interpolated to a time step $\Delta t = 0.1$ s and $\Delta z = \Delta y = 8$ m.

We examine the generated inflow characteristics in the following. The shear profile of U_∞ along the height z is generally described by the power-law as:

$$U_\infty(z) = \bar{u}_{ref}\left(\frac{z}{z_{ref}}\right)^{\alpha}, \tag{10}$$

where $\bar{u}_{ref}$ is the wind speed at a reference height z_{ref} and α is the so-called power-law exponent. The α exponent is a bulk parameter which includes both the effect of atmospheric stability and surface roughness z_0 [69,70]. The DNV-RP-C205 standard [71] recommends a value of $\alpha = 0.12$ in open seas with waves, which is in the range of the exponent of the two incoming inflows, I1 and I2, in this work, presented in Table 4. Fig. 3(a) presents the shear profile of the longitudinal wind speed component, normalized by the undisturbed incoming wind speed at hub-height $U_{\infty,z_{HH}}$, and computed as the average along the rotor span, i.e. $-D/2 < y < D/2$, for every height. The two incoming wind fields also differ in turbulence intensity level (TI), which is defined as:

$$\mathrm{TI} = \frac{\sigma_u}{U_{\infty,z_{HH}}}, \tag{11}$$

where $U_{\infty,z_{HH}}$ is 9 m/s, for both inflow 1 and inflow 2, and σ_u is the standard deviation of the longitudinal wind speed component, computed as the average of the standard deviations of the points along the rotor span ($-D/2 < y < D/2$) for every height. Fig. 3(b, c and d) presents the average of the standard deviation computed across the rotor ($-D/2 < y < D/2$) for every height, of the longitudinal, lateral and vertical wind speed components with height z. The relationship between the longitudinal, lateral, and vertical components at hub-height is presented in Table 4, together with the α exponent and the TI of the two turbulent inflows. The values of σ_v and σ_w are only slightly different from the values of $\sigma_v = 0.85\sigma_u$ and $\sigma_w = 0.60\sigma_u$ provided in the IEC standards [72], for neutral atmospheric conditions, and low terrain complexity, which would correspond to an open sea with waves. Furthermore, the standard deviation is seen to barely vary with height. The power spectral density (PSD) of the three wind speed components for the two inflows is presented in Fig. 4, where the decrease in energy as the frequency increases is observed. The dashed black and red lines in Fig. 4(a), for the U-component, represent the IEC Kaimal spectra [72], for the two inflows with different turbulence levels, respectively. If the Kaimal spectra are compared to the corresponding ones related to the conditions in this work, the former underestimate the frequency content at the lowest frequency range.

Table 4
Power-law exponent α, turbulence intensity TI, and standard deviation of v and w, σ_v and σ_w, as a function of σ_u, the standard deviation of the longitudinal wind speed component, of the two turbulent inflow wind fields, inflow 1 (I1) and inflow 2 (I2).

	α [–]	TI [%]	σ_v	σ_w
I1	0.08	6.1	0.71 σ_u	0.64 σ_u
I2	0.13	9.3	0.65 σ_u	0.57 σ_u

3.4. Computational domain and numerical parameters set-up

3.4.1. Large eddy simulation (VFS-Wind)

The computational domain employed for the large eddy simulation of wind turbine wakes is illustrated in Fig. 5. The size of the computational domain is $L_x \times L_y \times L_z = 14D \times 7D \times 1$ km, in streamwise (x), transverse (y), and vertical (z) directions, respectively. The origin of the coordinates coincides with the wind turbine footprint on the ground. The boundary conditions of the computational domain are presented in Table 5 and are described as follows. Turbulent inflows, generated from the previous simulations, are prescribed at the inlet ($x = -3.5D$) as the Dirichlet boundary condition. At the outlet ($x = 10.5D$), a Neumann boundary condition is applied to all velocity components ($\partial u_i/\partial x = 0$). The lateral and top boundaries enforce the free-slip condition, which ensures non-penetration for the velocity components in the wall-normal direction and a zero-gradient condition for the remaining components. The bottom boundary implements a non-penetration condition for the wall-normal velocity, along with a logarithmic rough wall function for the tangential velocities [66]. This representation allows for the relaxation of the grid resolution near the ground by considering equivalent shear stress for the ground surface. The domain is discretized by a Cartesian grid with grid nodes of $N_x \times N_y \times N_z = 281 \times 281 \times 105$. The grid is uniform in the x, y-directions with grid spacing $\Delta x = D/20$ and $\Delta y = D/40$. In the z-direction, the grid is uniform near the ground ($z \in (0, 2D)$) with $\Delta z = D/40$, and is gradually stretched to the top boundary. The time step is fixed at $\Delta t = 0.06$ s. This discretization has been shown to produce grid-independent turbulence statistics of wind turbine wake by a recent study on a similar case [28].

3.4.2. DWM (FAST.Farm)

The numerical domain in FAST.Farm, outlined in Fig. 6, is a Cartesian grid, which is $L_x \times L_y \times L_z = 10D \times 6D \times 0.6$ km, in streamwise (x), transverse (y), and vertical (z) directions, respectively. Two

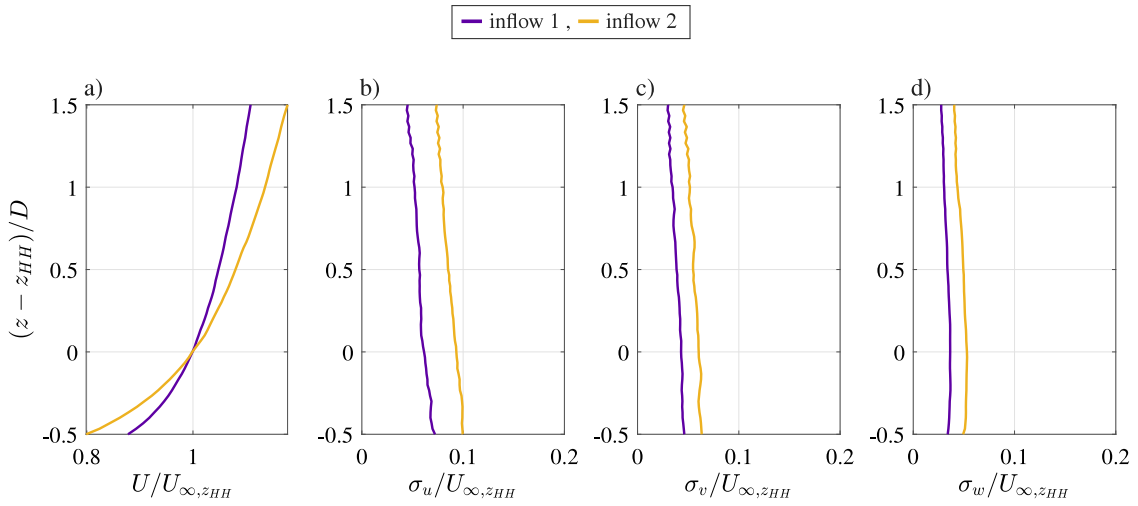

Fig. 3. Time-averaged turbulent inflow characteristics for the two inflows: (a) shear profile of the longitudinal component U; (b, c, d) standard deviation of the longitudinal, transverse and vertical components, σ_u, σ_v and σ_w, respectively. All the values are normalized by the undisturbed incoming wind speed at hub-height $U_{\infty,z_{HH}}$.

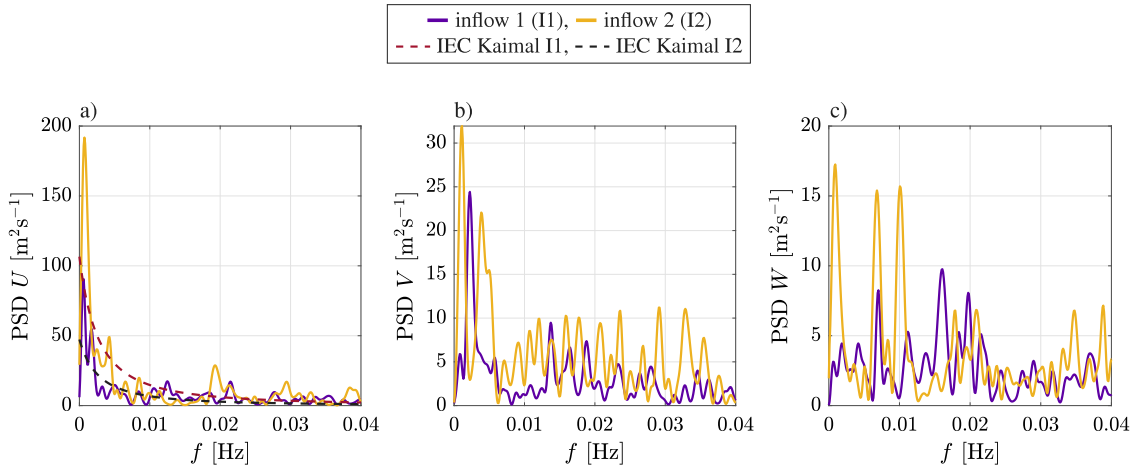

Fig. 4. Power spectral density (PSD) of the longitudinal U (a), lateral V (b) and vertical W (c) -components of the wind speed at hub-height, for the two inflows. The red and black dashed lines in (a) represent the IEC Kaimal spectra for inflow 1 and 2.

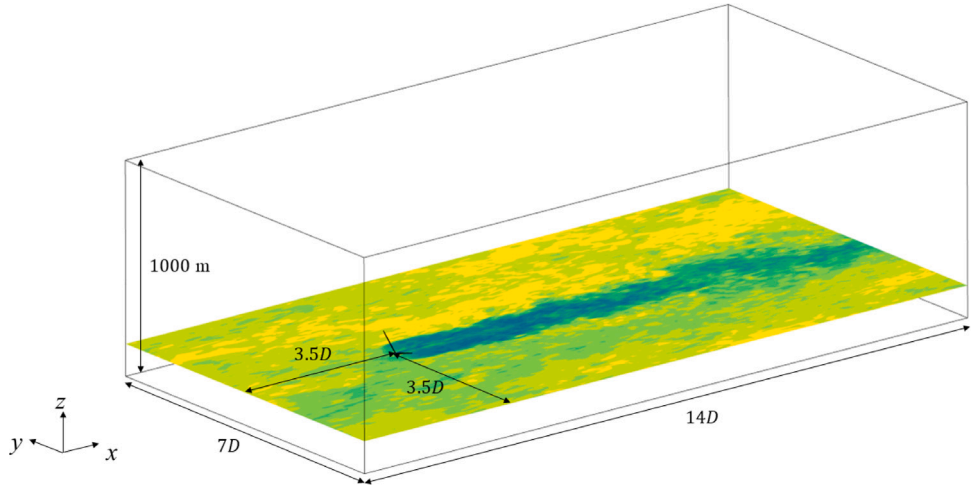

Fig. 5. Computational domain of the large eddy simulation in VFS.

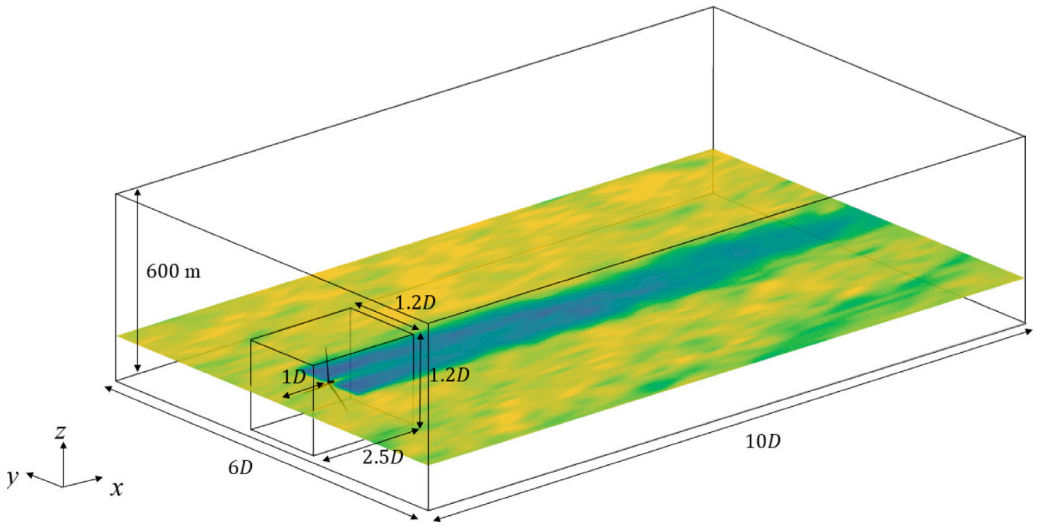

Fig. 6. High- and low-resolution computational domains in FAST.Farm.

Table 5
Boundary conditions employed for the large eddy simulations of the wake. .

No.	Boundary	Location	Boundary condition
1	Inlet	$x = -3.5D$	Dirichlet B.C. : Imposed value for u, v, w
2	Outlet	$x = 10.5D$	Neumann B.C. : $\frac{\partial u}{\partial x} = \frac{\partial v}{\partial x} = \frac{\partial w}{\partial x} = 0$
3	Sides	$y = \pm 3.5D$	Free slip: $v = 0$ and $\frac{\partial u}{\partial y} = \frac{\partial w}{\partial y} = 0$
4	Top	$z = 1$ km	Free slip: $w = 0$ and $\frac{\partial u}{\partial z} = \frac{\partial v}{\partial z} = 0$
5	Bottom	$z = 0$	Wall normal components: $w = 0$ Wall shear stress: $\tau = \rho(u^*)^2$ with $\frac{u_t(z_p)}{u^*} = \frac{1}{\kappa} \ln\left(\frac{z_p}{z_0}\right)$

Note: $u_t(z_p)$ denotes the tangential velocity (parallel to the wall) at the wall-adjacent grid with a height of z_p. z_0 denotes the roughness length, which is set according to the terrain type [73]. $\kappa \approx 0.4$ is the von Kármán constant.

sub-domains are defined: the larger domain, corresponding to the low-resolution domain, and the smaller domain around the rotor, representing the high-resolution domain. The low-resolution domain has the same dimensions as the entire domain. The turbine is placed at $x = 1D$, inside the high-resolution domain, which is $1.2D$ wide and high, and it extends over $2.5D$ in the longitudinal direction. The resolution of each domain, based on the work of Shaler et al. [74], is presented in Table 6, where dSLow is the resolution in y, z-directions in the low-resolution domain, and dSHigh the corresponding one in the high-resolution domain. The time steps for both domains, dtLow and dtHigh, are presented in Table 6. The recommended values by Shaler et al. [74] are indicated as *Rec.*, whereas the ones used in this work are the *Used* ones. The time step in the high-resolution domain is determined by f_{max}, which indicates the highest frequencies influencing the structural excitation. c_{max} is the maximum blade chord length of the turbine, and it defines the spatial resolution in y, z-directions of the high-resolution domain, dSHigh. In the current work, the chosen resolution is above the recommended value of 5.8 m. However, since the focus of this research is not on the structural analysis of the wind turbine, combined with the fact that this one coincides with the resolution of the LES data, a dSHigh of 8 m is considered to be sufficient.

The influence of the nacelle on the time-averaged and the instantaneous wake characteristics, and on the wake meandering statistics, is included in the LES model, but not in the DWM model. Several studies (e.g. [75–78]) have demonstrated that modeling the tower and nacelle affects the near-wake region under uniform incoming flow, and large nacelle- or tower-to-rotor diameter ratios. However, in the current case, the focus of the study is on the far-wake, for turbulent inflow conditions. Therefore, including the nacelle in the modeling should have a weak influence on the far-wake velocity deficit in the current case. For the same reasons, the tower was not modeled for the current analyses in either of the models. Additionally, the ratios of rotor diameter-to-tower-diameter and -to-nacelle diameter are large enough to decrease the effect that modeling these would have in the far-wake region for a turbulent incoming inflow. To verify that the tower's effect at the distance of interest ($8D$) is small, three cases are analyzed, i.e. with zero yaw or tilt angle ($\gamma = \beta = 0$), and one yaw case ($\gamma = 30°$, $\beta = 0$) and one tilt case ($\gamma = 0$, $\beta = 15°$), under inflow I1. In Appendix, the instantaneous velocity, the time-averaged velocity deficit, and the wake meandering statistics, are presented for these cases with and without the tower model.

4. Comparison of DWM against LES

This section systematically analyzes the predictive capability of the dynamic wake meandering (DWM) model by comparing it with the large eddy simulation (LES) data. The analysis focuses on various wake quantities, including the time-averaged wake deficit in Section 4.1, and wake meandering statistics such as the time-averaged position and standard deviation of the wake center (meandering amplitude) in Section 4.2. Please note that in this section, the filter size parameter of the DWM (C_{meand}) is tuned to generate the best agreement with LES in the far-wake ($x = 8D$), as indicated in Table 2. The effect of this parameter will be further discussed in Section 5.

4.1. Time-averaged wake

This subsection investigates the predictive capacity of the DWM model for the average wake deficit over time. The wake is analyzed separately for yaw and tilt: while the phenomenon of wake deflection appears similar in both cases, the wake deflection induced by tilt is also affected by the vertical shear and the ground effect, which increases the intricacy of wake modeling.

4.1.1. Horizontal wake steering

The predictive capability of the DWM model for cases with yaw misalignment is firstly examined by the time-averaged contour plots at the hub-height plane for three representative yaw angles, $\gamma = 0°$, 15° and 30°, as shown in Fig. 7, for inflow 1. The C_{meand} filter used in the results shown in this section corresponds to the values in Table 2, cases

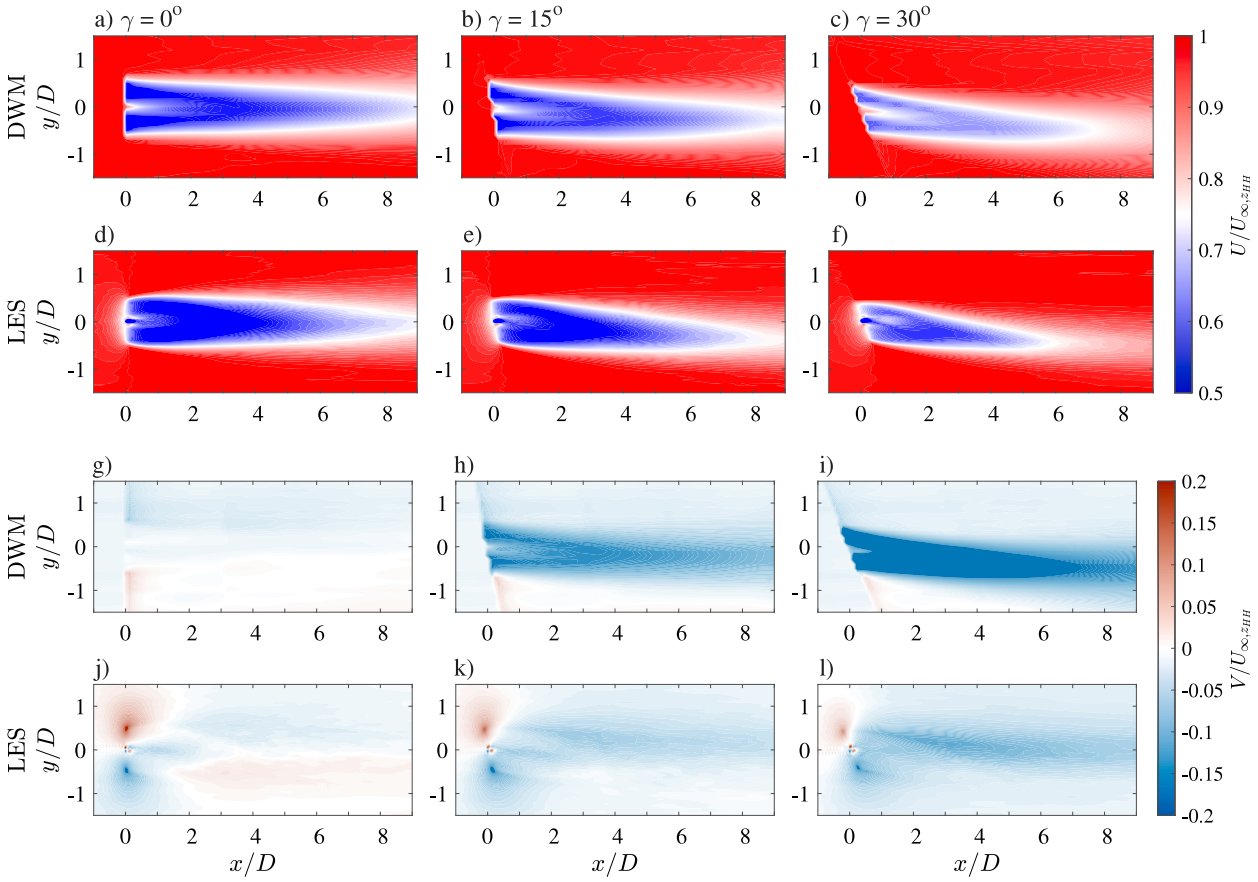

Fig. 7. Time-averaged velocity at the horizontal (xOy) plane at hub-height for three representative yaw deflection angles $\gamma = 0°$, $15°$, $30°$, for inflow 1; (a–c) streamwise velocity $U/U_{\infty,z_{HH}}$ computed by the DWM model, and (d–f) by LES; (g–i) horizontal velocity $V/U_{\infty,z_{HH}}$ computed by the DWM model, and (j–l) by LES.

Table 6
Recommended and used values for the spatial and time resolution in the FAST.Farm numerical domain. f_{max} is the highest frequency influencing the structural response and c_{max} the maximum blade chord length.

dtLow [s]		dtHigh [s]		dxLow [m]		dSLow [m]		dxHigh [m]		dSHigh [m]	
Rec.	*Used*	*Rec.*	*Used*	*Rec.*	*Used*	*Rec.*	*Used*	*Rec.*	*Used*	*Rec.*	*Used*
$< \frac{C_{\text{meand}} D_w}{10 U_{\infty,z_{HH}}}$		$< \frac{1}{2 f_{max}}$				$< \frac{C_{\text{meand}} D_w U_{\infty,z_{HH}}}{150\text{m/s}}$				$< c_{max}$	
<5.0	3.0	<0.5	0.2	$0.11D$	$0.11D$	$<0.12D$	$0.10D$		$0.0075D$	<5.8	8.0

1a to 4a, which lead to the best match of the DWM model to the LES data.

Fig. 7(a to c) presents the streamwise component of the wind velocity U predicted by the DWM model. Fig. 7(d to f) shows the same results, as obtained with LES. The streamwise velocity predicted by both approaches is similar. For all yaw angles, both models provide a consistent streamwise development of the wake, characterized by the expansion of the wake and the recovery of the streamwise velocity due to the turbulent mixing and wake meandering mechanism [79]. As the yaw misalignment angle increases, the wake deficit and the width of the low-speed region both decrease for both models, due to the decrease of thrust, and of the projected rotor area. In both models, the streamwise component of the velocity field is approximately symmetric with respect to the wake centerline.

Some minor discrepancies between the models are also observed. The first difference between the two models for a zero yaw angle is at the near-wake region, as shown in Fig. 7(a) and (d). In the DWM model, the width of the low-velocity region starts to decrease linearly right behind the rotor ($x = 0$). In contrast, the near-wake region predicted by LES has a constant width up to approximately two rotor diameters downstream ($x = 2D$). From that point on, the decrease of the wake deficit and the width of the low-speed region is slightly slower for the DWM model. The same trend is also observed for $\gamma = 15°$ and $30°$, when comparing Fig. 7(b–c) and (e–f).

However, the lateral velocity component (V) in the wake predicted by both approaches shows a more significant discrepancy, when Fig. 7(g–i) and (j–l) are compared. For the case with $\gamma = 0°$, the time-averaged transverse velocity V is symmetric to the wake centerline and is almost zero for both cases. In the far-wake, both models predict a converging pattern of the transverse velocity, reflecting a mean convection from the freestream to the wake and thus contributing to the wake recovery. It is worth noting that LES predicts a diverging transverse velocity at the rotor position $x = 0$ in Fig. 7(j), which reflects the initial wake expansion, as a result of mass conservation [63]. Such an initial wake expansion is not captured by the DWM model, because its governing equation (3) for the wake deficit is simplified with the far-wake assumption without imposing the continuity condition. As the yaw misalignment increases, the transverse component increases, and the symmetry with respect to the centerline vanishes. Furthermore, the induced velocity increases in the negative y-direction, and its magnitude increases with γ. Fig. 7(h), and especially (i), indicates an overestimation of the mean value of the transverse component V in

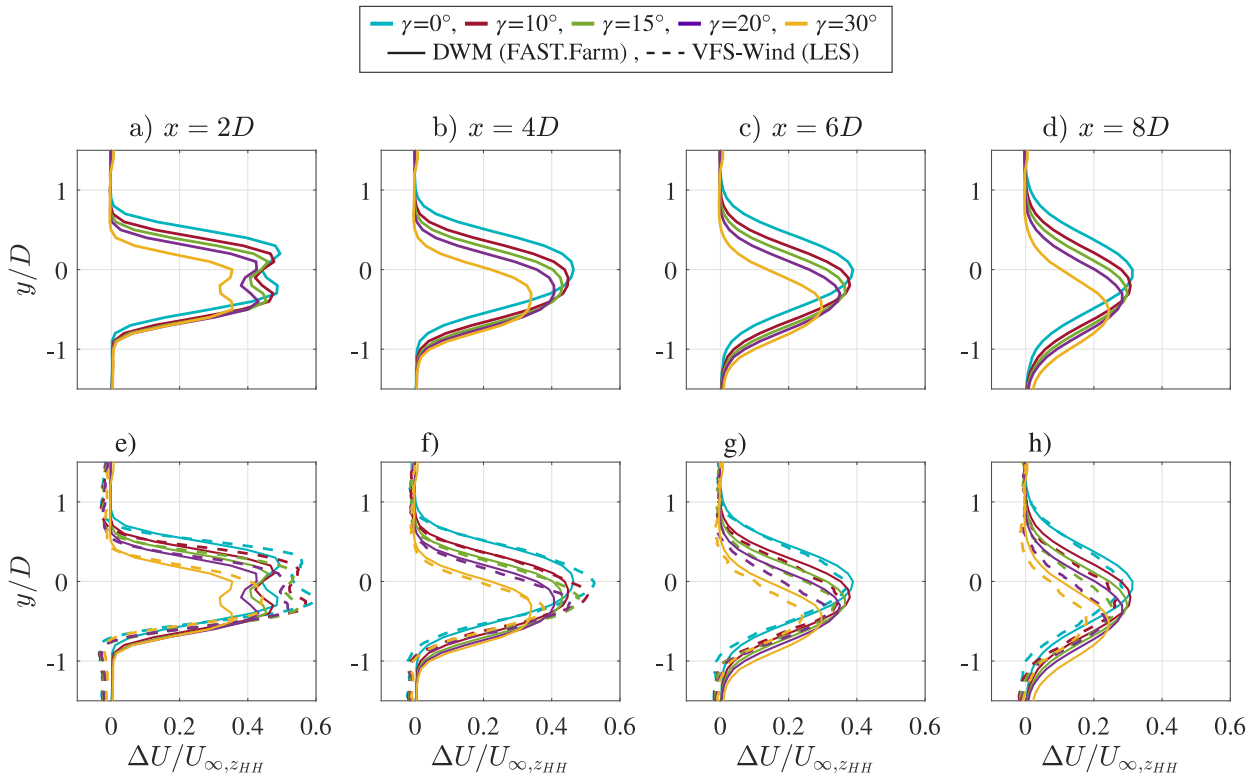

Fig. 8. Time-averaged velocity deficit $\Delta U(y)/U_{\infty,z_{HH}}$ at $x = 2,\ 4,\ 6$ and $8D$, at the hub-height plane for the five yaw deflection angles γ, for inflow 1; (a–d) is computed by the DWM model, and (e–h) by LES, with dashed lines. The thin lines show the DWM results (same as a to d), for the simplicity of the comparison.

the DWM model with respect to that of LES. Besides the magnitude, the transverse components predicted by both models reside in different locations. In the result of DWM, V resides in the same region with the wake deficit. However, the present LES results as well as previous experiments [7] and simulations [28] suggest that the transverse velocity should be skewed towards the wake border behind the rotor leading edge. This difference indicates that the wake deflection in the DWM model is driven only by the transverse velocity component created directly in the near-wake, with other physics leading to the wake centerline deflection, e.g., the wake deformation [9], being ignored.

In Fig. 8, the time-averaged wake is examined in further detail by showing the horizontal wake deficit profiles. Fig. 8(a to h) presents the wake deficit $\Delta U(y)/U_{\infty,z_{HH}}$, with $\Delta U(y) = U_{\infty,z_{HH}} - U(y)$, at the hub-height. The results are presented at four downwind locations, $x = 2,\ 4,\ 6$ and $8D$, for the yawed rotor with five γ angles. The solid lines, in the top row (a to d), represent the deficit as computed by the DWM model. The deficits computed by LES, with dashed lines, are shown in the bottom row (e to h), together with the DWM results, i.e. the same as shown in the top row (a to d), outlined by thinner lines, to make the comparison between the models more clear. Similar trends are observed for both models: both the wake width and deficit decrease as the yaw angle increases. The DWM model predicts a lower deficit at the near-wake region than LES, i.e. at $x = 2D$. As the downstream distance x continues to increase beyond $x \geq 6D$, the wake deficits become similar for both models, and resemble a Gaussian shape symmetric to the summit of the wake deficit [7].

Further, the similarity of the wake deficit between cases with different yaw angles is examined. Li and Yang [28] suggested that there is a similarity of wakes for turbines with different yaw angles based on large eddy simulations of a 2.5 MW wind turbine. Based on that work, the time-averaged wake velocity deficit profiles $\Delta U(y)$ for cases with different yaw angles collapse if $\Delta U(y)$ is normalized by a proper velocity (U_N) and length (R_N) scale, derived based on one-dimensional momentum theory in the streamwise direction. The characteristic velocity and length are defined as follows:

$$U_N = U_{\infty,z_{HH}} \left(1 - \sqrt{1 - \widetilde{C}_T \cos^2\gamma}\right), \tag{12}$$

and

$$R_N = R\cos\gamma \sqrt{\left(1 + \sqrt{1 - \widetilde{C}_T \cos^2\gamma}\right) \Big/ \left(2\sqrt{1 - \widetilde{C}_T \cos^2\gamma}\right)}. \tag{13}$$

With the above characteristic scales, the results for different yaw angles predicted by both methods can be compared quantitatively, as in Fig. 9, which shows the deficit shifted by the wake centers y_c, and normalized by the characteristic velocity U_N and R_N. A good agreement between the models is observed in the normalized transverse profiles of the streamwise component beyond the near-wake region $x = 2D$. This collapse also indicates that the velocity deficit profiles are almost symmetric with respect to the wake centerline for every yaw misalignment angle and the similarity of wake for wind turbines operating at different yaw angles is well captured by both DWM and LES. A small discrepancy between the normalized wake deficit profiles is observed, where the wake deficit predicted by the DWM model is larger than LES, in the far-wake ($x = 8D$), and especially for the largest yaw deflection angle. This difference is explained, and consistent, with the observation from the contour plots in Fig. 7.

Although these results pertain specifically to inflow 1, which corresponds to the lower turbulence intensity level, similar comparative trends between the LES and DWM model results are also evident for inflow 2. However, for the sake of conciseness, these results are not presented in this paper. The substantial agreement observed in both cases showcases the predictive capabilities of the DWM model for the time-averaged wake deficit and its shape on the hub-height plane, even when considering relatively large yaw angles.

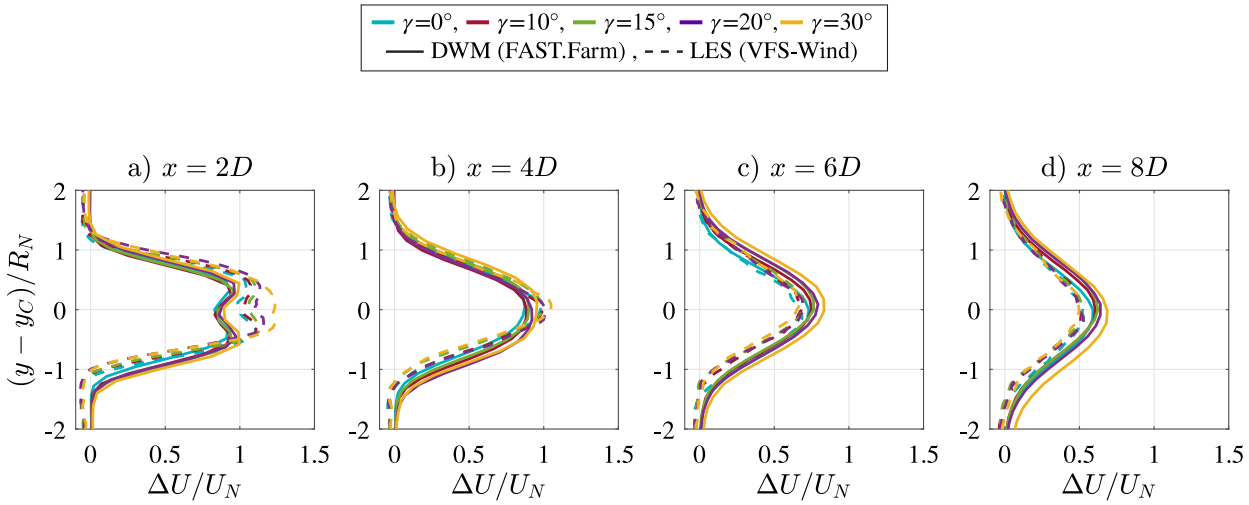

Fig. 9. Time-averaged velocity deficit ΔU at $x = 2,\ 4,\ 6$ and $8D$, at the hub-height plane for the five yaw deflection angles γ, for inflow 1. The profiles are normalized by U_N, and the wake centers shifted with respect to y_c and normalized by the length scale R_N.

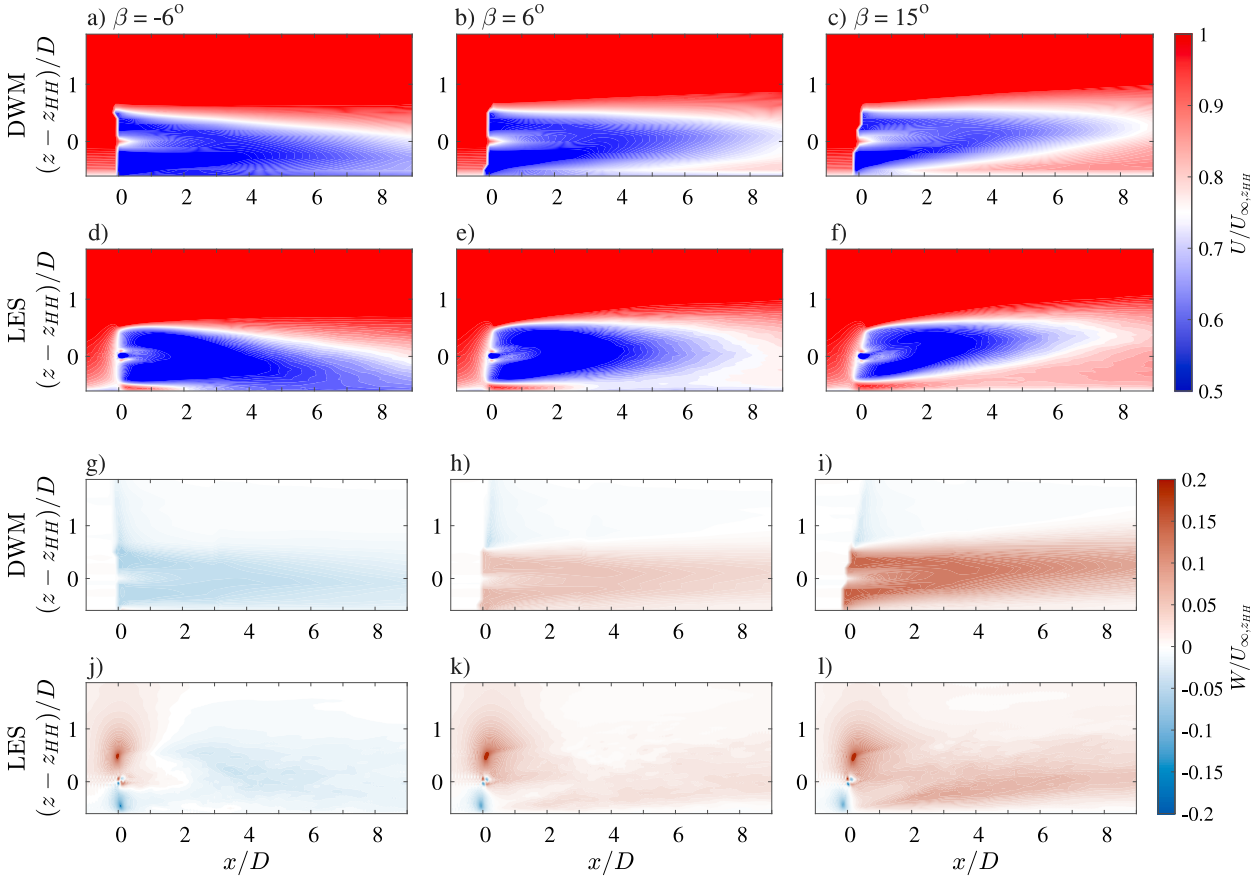

Fig. 10. Time-averaged velocity on the vertical (xOz) plane for three representative tilt deflection angles $\beta = -6°,\ 6°,\ 15°$, for inflow 1; (a–c) streamwise velocity $U/U_{\infty,z_{HH}}$ computed by the DWM model, and (d–f) by LES; (g–i) vertical velocity $W/U_{\infty,z_{HH}}$ computed by the DWM model, and (j–l) by LES.

4.1.2. Vertical wake steering

Fig. 10(a to c) presents the contour of the time-averaged streamwise wind speed $U(z)$, normalized by the undisturbed incoming wind speed at hub-height $U_{\infty,z_{HH}}$, at the vertical plane (xOz) for three tilt misalignment angles, namely $\beta = -6°$, 6° and 15°, for the DWM model. The same results are shown for LES in Fig. 10(d to f). In general, there is good agreement in the vertical deflection predicted by both the DWM model and LES data. For the negative tilt angle ($\beta = -6°$), the wake deficit is deflected downwards as the distance downstream increases. On the other hand, for positive tilt angles, the wake is deflected upwards. Both the velocity deficit and the width of the low-speed region decrease with increasing tilt angle, similar to the cases with yaw misalignment (Fig. 7). Once again, the initial wake width does not change until approximately $x = 2D$ for the LES model, whereas a linear decrease of the width of the low wind speed region is observed in the DWM model throughout the entire wake region. In the far-wake, the wake deficit in the LES is recovered at a higher rate, reflecting a stronger exchange of momentum with freestream flow predicted by the high-fidelity model.

The vertical velocity component $W(z)/U_{\infty,z_{HH}}$ is shown in Fig. 10(g–i) and (j–l) for the DWM model and for LES, respectively. For the case with the negative tilt angle, the vertical component is a small negative value, for both models. For the positive tilt angles, this component is positive. Again, the vertical velocity predicted by the DWM model has a larger magnitude than that predicted by LES. For the DWM model prediction, this vertical velocity originates from the rotor location, due to the rotor vertical thrust components, and slightly decreases in magnitude as it travels downstream. However, in the LES, the vertical component has a smaller magnitude in the near-wake, but increases slightly in magnitude as it travels downstream. Such a phenomenon, particularly apparent in Fig. 10 (l), indicates that the rotor vertical thrust may not be the only driving mechanism leading to a vertical wake deflection in LES. Other mechanisms, such as the kidney-shaped deformation in the wake [7], may also contribute to the upward deflection of the wake centerline. The absence of this more sophisticated flow mechanism in the DWM model is compensated by a stronger vertical velocity, as the parameter C_{meand} (see Table 2) is tuned to achieve the best match of the vertical wake deflection with LES in the far-wake ($x = 8D$). This explanation can account for the significant difference observed in the vertical velocity between the DWM model and LES data.

Fig. 11(a to h) presents the wake deficit $\Delta U(z)/U_{\infty,z_{HH}}$, with $\Delta U(z) = U_\infty - U(z)$, at $x = 2,\ 4,\ 6$ and $8D$, for the six tilt deflection angles. The solid lines, in the top row (a to d), show the deficit from the DWM model. As seen, the vertical profiles predicted by the DWM model are symmetric with respect to the wake center, and are cut off by the ground at $z = 0$. For $\beta = 0$, the wake center remains at the hub height (z_{HH}) at all downstream locations considered. The DWM model correctly predicts the trend of the wake vertical deflection, resulting in a higher wake center displacement with larger β. For the case with $\beta = -6°$, the wake center is deflected downwards. The decreasing trend of wake deficit via increasing the rotor misalignment ($|\beta|$) is also captured by the DWM model.

Fig. 11, (e to h), validates the predictive capability of the DWM model by comparing it to the results from LES. The figure displays the results predicted by the DWM and LES models using solid and dashed lines, respectively. Although the DWM model utilizes optimal values of C_{meand} to match the wake center position of LES at $x = 8D$, significant discrepancies are observed between the two approaches in terms of the wake deficit. The DWM model consistently overpredicts the deficit. For a tilt angle of $\beta = -6°$, the DWM model overpredicts the wake deficit by 22% at the wake center location. As the wake is deflected upwards with a positive tilt angle β, the difference between the model predictions decreases. For cases with $\beta = 20°$, the difference is reduced to 11%. The relatively larger prediction for cases with a negative tilt angle is attributed to the ground effect. In LES, the boundary condition limits the downward deflection of the wake, but this is not accurately modeled by the DWM.

4.2. Wake meandering statistics

Wake meandering refers to the overall motion of the wake, which plays a crucial role in the expansion of the time-averaged wake and the generation of unsteady wind velocity fluctuations within the wake [80]. In this subsection, we assess the predictive capability of the wake meandering of the DWM model by checking the statistics of the wake center motion.

To illustrate the wake meandering predicted by DWM, Fig. 12 presents the instantaneous flow field $U(y)/U_{\infty,z_{HH}}$ at the hub-height plane predicted by both the DWM model and LES, for yaw angles $\gamma = 0°$, 15° and 30° and for tilt angles $\beta = -6°$, 6° and 15°, at the same instant for inflow 1. The figure clearly reveals the similarities and differences of wake predicted by the two approaches of different modeling fidelity. The instantaneous wake contours predicted by both approaches show similar silhouettes. However, the instantaneous wake predicted by LES contains more turbulent flow structures at smaller scales, which are not resolved by the DWM model. This difference is attributed to the spatial filtering process that removes the small eddies of the inflow and the absence of the shear-layer instability mechanism in the DWM model. Based on these instantaneous wake fields, we define the instantaneous wake center position, $y_c(x)$ or $z_c(x)$, at a downstream location x as the center-of-mass of the wake deficit, as employed by Brugger et al. [59].

In the following, we will investigate the predictive capability of the DWM model by examining the characteristics of the wake center motion, focusing on the mean and standard deviation of the wake center. From a physics point of view, the mean value represents the time-averaged wake deflection, and the standard deviation represents the amplitude of the wake meandering motion. For cases without wake steering ($\gamma = \beta = 0$), the mean wake center position is known a priori, and only the standard deviation is of interest [19]. Here, by checking both the mean position and standard deviation of the wake center, we verify if both the mean deflection and the meandering can be predicted simultaneously in the DWM model.

Fig. 13 presents an overview of the mean and standard deviation of the horizontal and vertical positions of the wake center, y_c and z_c, respectively, at $x = 8D$. The mean and standard deviation of the horizontal deflection is shown for the yaw misalignment cases, whereas the mean and standard deviation of the vertical deflection is presented for the tilt angle cases. The statistical values of the wake meandering as computed with the DWM model are outlined by red circles, and the corresponding mean values for the LES model are depicted by blue triangles. Both the mean and standard deviation values are normalized by the rotor diameter. The hub-height z_{HH} is subtracted from the mean vertical deflection z_c.

The generally good agreement in Fig. 13 is obtained after adjusting C_{meand} to fit the mean and standard deviation values for each yaw misalignment and tilt deflection case, respectively, to the LES data. One key finding when comparing the wake meandering statistics of the DWM model and LES is that the results of the former are sensitive to the filter size to calculate the spatial-averaged velocity that is used to meander the wake in this model. The present results are obtained with the C_{meand} filter size presented in Table 2 that result in the closest mean and standard deviation compared to LES data at $8D$. The optimal C_{meand} is found to be different for cases with different yaw and tilt angles.

For the statistics of the horizontal wake center meandering, the optimal is found in the range $1.90 < C_{\text{meand}} < 2.10$, which is close to the default value $C_{\text{meand}} = 2$ proposed by Larsen et al. [19]. The largest difference between the models in the mean value of the wake deflection at $x = 8D$, for the yaw misalignment case, Fig. 13(a), is for $\gamma = 15°$, for which the DWM model overestimates the mean value, for I2, by 15%. The standard deviation is overestimated by the DWM model, especially for the 4a case, $\gamma = 30°$, where the value is 25% higher. However, this is the closest achievable value by the DWM model for the standard deviation σ_{y_c}, as compared to the LES

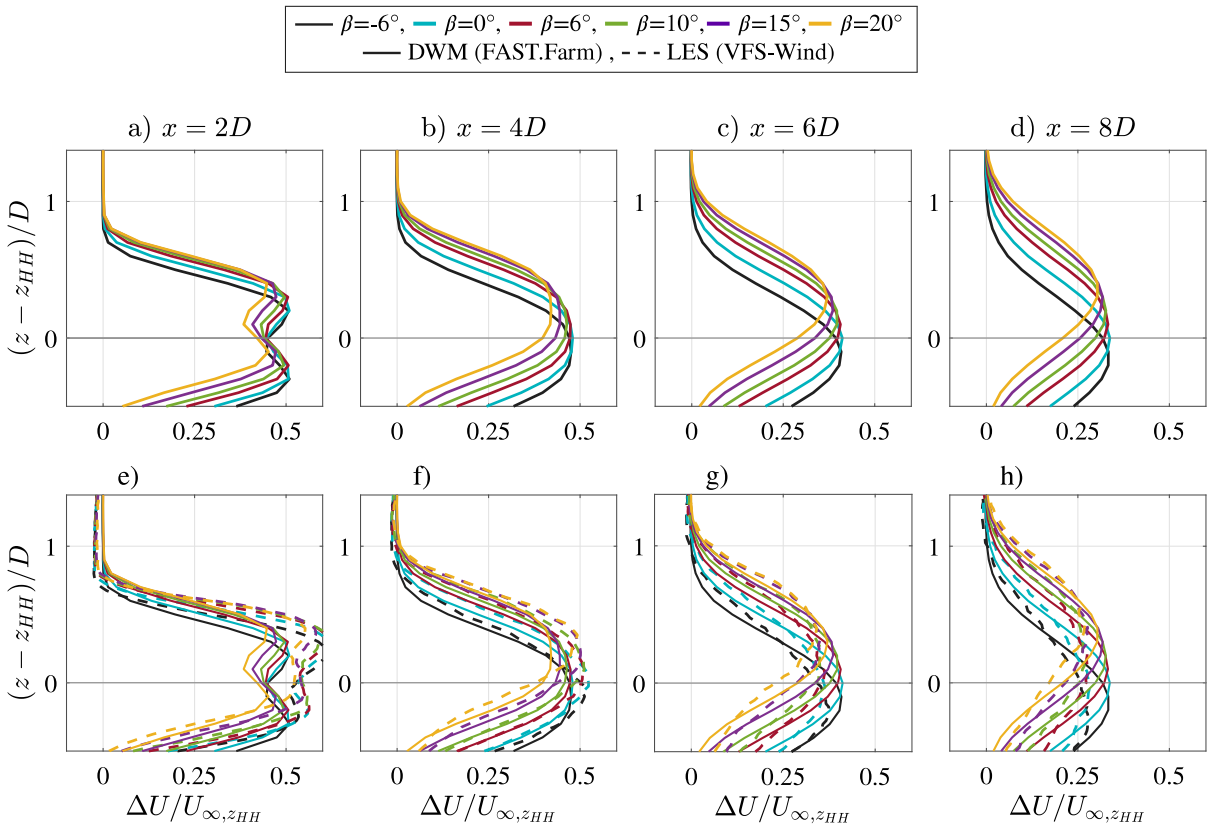

Fig. 11. Time-averaged velocity deficit $\Delta U(z)/U_{\infty,z_{HH}}$ at $x = 2,\ 4,\ 6$ and $8D$, for $-0.5D < (z - z_{HH}) < 1.3D$, at the rotor plane for the six tilt angles β, for inflow 1; (a–d) is computed by the DWM model, and (e–h) by LES. The hub-height is at $(z - z_{HH})/D = 0$, outlined by the solid horizontal line. The thin lines show the DWM model results same as (a) to (d), for the simplicity of the comparison.

results, without compromising the mean value of the horizontal wake meandering $\bar{y}_c$ for this specific case. The larger the C_{meand} filter, the larger the filter area used to calculate the spatial-averaged velocity with which the wake planes meander becomes. A larger polar grid implies that the convection velocity will be computed by involving a larger portion of freestream velocity and the wake deficit will have a smaller contribution when taking the average on the polar grid, resulting in a larger U related to the meandering of the wake plane. The larger averaged U-component yields a smaller V/U ratio, and therefore a smaller mean and standard deviation of the wake center. Therefore, although reducing this filter would yield a closer result of the standard deviation to the LES results, it would also decrease the mean deflection and make a large error in Fig. 13(a).

On the other hand, the optimal value of C_{meand} is significantly larger for predicting the mean vertical deflection of the wake for a tilted rotor, as shown in Table 2. It is found that the time-averaged wake center deflection $\bar{z}_c$ can be well predicted by the DWM for cases with $\beta \geq 6°$compared to LES; however, a remarkable difference between both models is found for the cases $\beta = -6°$ and $\beta = 0°$, and cannot be further reduced by adjusting C_{meand}. This difference in σ_{z_c} is related to the ground effect, which limits the vertical downward deflection of the wake, and is only modeled in large eddy simulations. Moreover, for the inflow considered in this study, the mean value of the vertical meandering is barely affected by the turbulence intensity for either of the models. The TI is found to not affect remarkably the standard deviation of the vertical meandering of the wake center σ_{z_c}, in the LES calculations, but has a larger impact for the DWM model. Moreover, it is found that the DWM model predicts a weaker wake meandering, implying that a smaller vertical velocity fluctuation is obtained for these large C_{meand} values.

Furthermore, Fig. 13, (c) and (d), shows that for both models, the standard deviation of the vertical meandering is smaller than that of the horizontal meandering, due to the lower standard deviation of the vertical component, σ_w, with respect to that of the lateral one, σ_v, which is consistent with the velocity fluctuations of the inflow as shown in Fig. 3, (c) and (d).

5. Discussion on the limitations of the DWM model

As presented in the previous section, when comparing the wake meandering statistics of the DWM model and LES, the results of the former show a dependence on the filter size employed to calculate the spatial-averaged velocity that is used to advect the wake, represented by the C_{meand} parameter (see Section 2.2). This section aims to reflect on the differences of the DWM model results compared to the LES data, focusing on the effect of the filter size. Two main limitations based on the current findings of the comparison of the DWM model against LES are addressed and analyzed in the following. Additionally, the power available in the wake at $x = 8D$ is presented for both LES and the DWM model.

5.1. Dependence of the mean wake deflection on C_{meand}

The first limitation of the present DWM model is that the mean wake deflection is dependent on the value of C_{meand}, and the optimal value is found to vary with the yaw/tilt angles, as shown in Table 2. Increasing C_{meand} is required to fit the wake deflection with increasing misalignment angles, since by increasing the C_{meand} value, i.e., having a larger filter size, the filtered averaged streamwise velocity also increases, leading to the decrease of the ratio between the perpendicular and the streamwise velocity components.

Secondly, the optimal C_{meand} value in the DWM model is also dependent on the downstream location x, so C_{meand} is tuned with different values if the DWM and LES models are compared at different locations

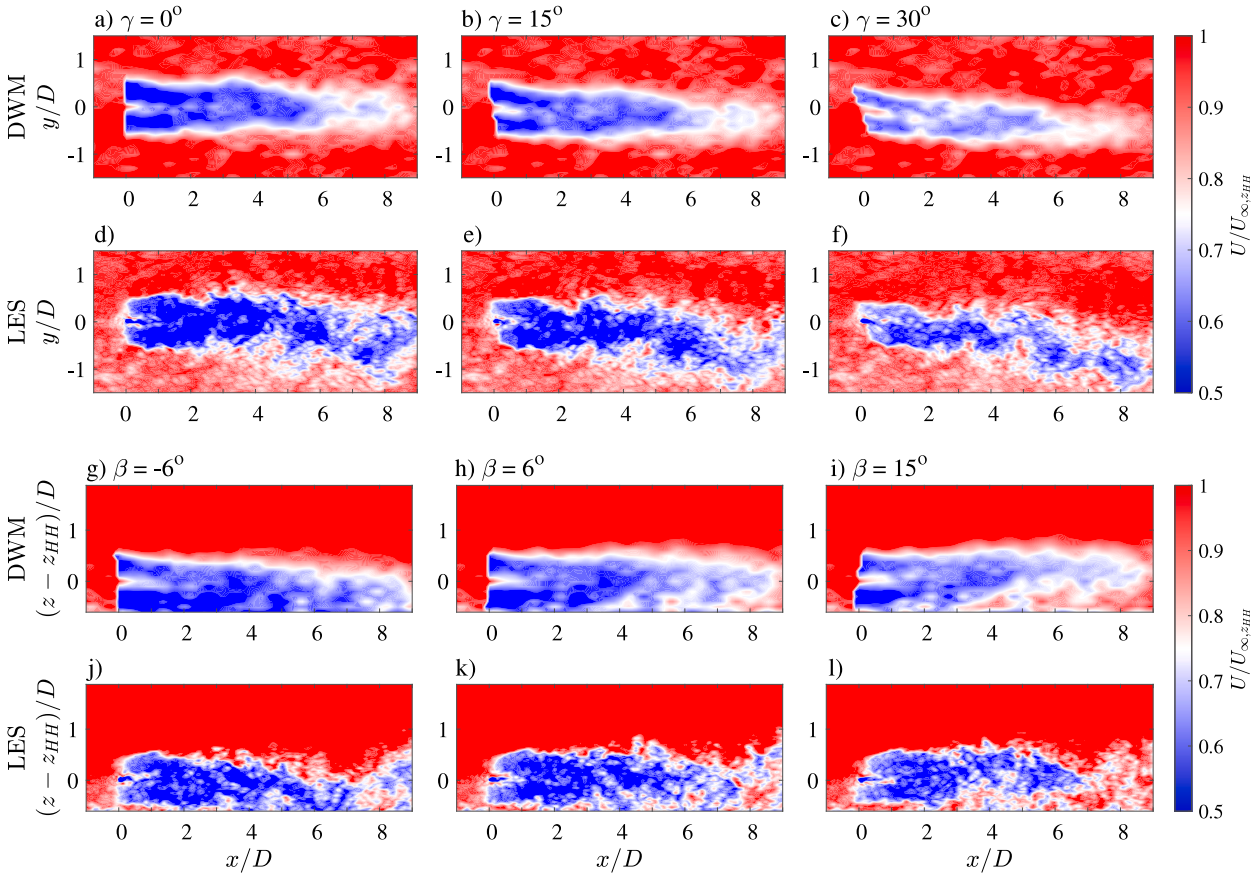

Fig. 12. Instantaneous flow field for $\gamma = 0°$, 15° and 30° and $\beta = -6°$, 6° and 15°, for inflow 1; (a–c) streamwise velocity $U/U_{\infty,z_{HH}}$ at the hub-height plane xOy computed by DWM, and (d–f) by LES; (g–i) streamwise velocity $U/U_{\infty,z_{HH}}$ at the xOz plane computed by DWM, and (d–f) by LES.

Table 7
Fitted C_{meand} filter values based on the results at $x \in (2, 8D)$, for inflow 1, for the cases with yaw deflection.

Case ⟶	1a	2a	3a	4a
C_{meand} @ $x = 2D$	2.10	2.20	2.20	2.30
C_{meand} @ $x = 4D$	2.10	2.20	2.20	2.30
C_{meand} @ $x = 6D$	2.00	2.10	2.10	2.20
C_{meand} @ $x = 8D$	1.90	2.00	2.00	2.10

x. In other words, the C_{meand} tuned with the data at $x = 8D$ does not guarantee the best fit of the two models at a different downstream location. Fig. 14 presents the mean values of the horizontal and vertical deflection of the wake at $x = 2,\ 4,\ 6$ and $8D$, for inflow 1. The LES data are shown by blue triangles. The red circles represent the best fit of the DWM model at different downstream locations, using the C_{meand} values presented in Table 7. The markers for the two models go from lighter to darker, as the deflection angles γ or β increase. For the cases with a yaw angle, as the distance downstream decreases, the size of the polar grid, increases: for instance, for $\gamma = 10°$, at $x = 8D$, the filter is equal to 1.90, whereas at $x = 6D$, C_{meand} is 2.00. Consequently, the filter for each case and location is adjusted depending on the downstream distance x, for $x/D \in (2, 8)$. For the vertical wake deflection cases, it was found that the filter parameter at different downstream locations did not vary with downstream distance, i.e. the filter remains constant with x, see Table 2, for the different tilt angle cases.

For $x \geq 2D$, the maximum difference in the mean horizontal deflection is 7.4%, for $x = 8D$ and $\gamma = 15°$. At $x = 2D$, the mean deflection values computed by the DWM model are overestimated, which is consistent with the fact that the near-wake modeling equations in the DWM model are simplified with the far-wake model assumption. As the downstream distance increases, the mean values of the DWM model compare better to those of LES. The estimation for the mean horizontal deflection in this work is in agreement with the values predicted by the analytical model for the far-wake from [12], depicted by the dotted lines in Fig. 14(a), for the different yaw misalignment cases. This model was validated against field measurements by Brugger et al. [81]. As such, the comparison of the results in the current work to the predicted values by Qian and Ishihara's model, can serve as a basis for the validation of the current results.

Regarding the mean vertical wake deflection, for tilt angles of $\beta = 10°$, 20°, and 30°, the values are similar to the mean horizontal deflection for yaw angles of $\gamma = 10°$, 20°, and 30°. However, there is a notable difference in the cases of $\beta = 0°$ and $-6°$. This discrepancy highlights the challenge of using the DWM model as a predictive approach for vertical wake steering, particularly in cases with negative tilt angles and downward wake deflection. Nevertheless, it is important to consider such scenarios as downward wake deflection has the potential to enhance the wind speed for downwind turbines [17]. This difference may be attributed to the ground effect, which is implicitly imposed by the boundary conditions in the LES but is not considered in the employed DWM model. The analysis for inflow 2 is very similar to that of inflow 1, and therefore is not presented for conciseness.

5.2. *Effect of the C_{meand} on the wake meandering motion*

Another limitation of the DWM model, based on the analyses in this work, is revealed by the time series and power spectral densities of the wake center meandering, which are found to be dependent on the C_{meand} filter, and show a remarkable difference from the LES data.

Fig. 15 presents the time series and power spectral density of the horizontal meandering of the wake center y_c for case 0, i.e., $\gamma = \beta = 0°$.

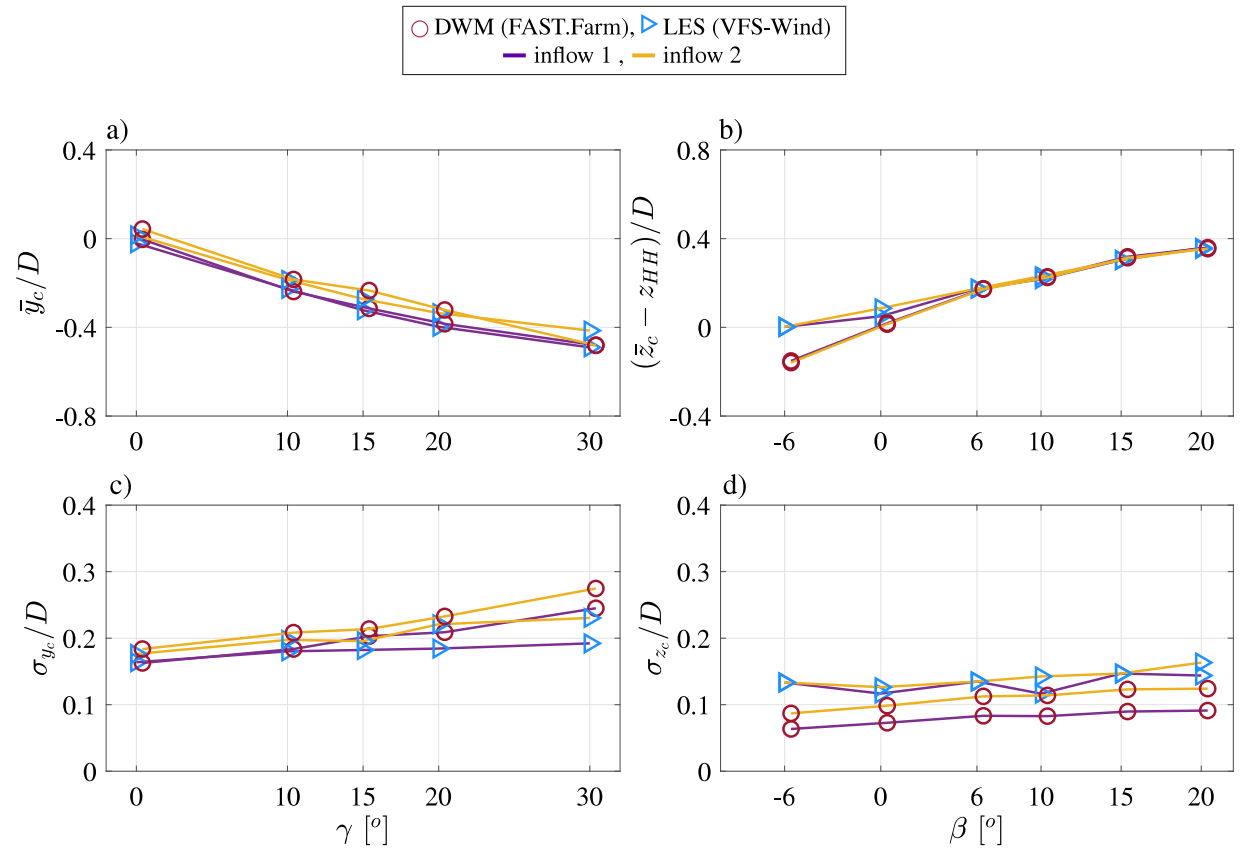

Fig. 13. Mean horizontal and vertical position, $\bar{y}_c$ and $\bar{z}_c$ (a, b) and standard deviation σ (c, d) of the wake center position at $8D$ for the yaw and tilt misalignment cases, respectively, for inflow 1 and inflow 2. The hub-height z_{HH} is subtracted from the mean vertical deflection.

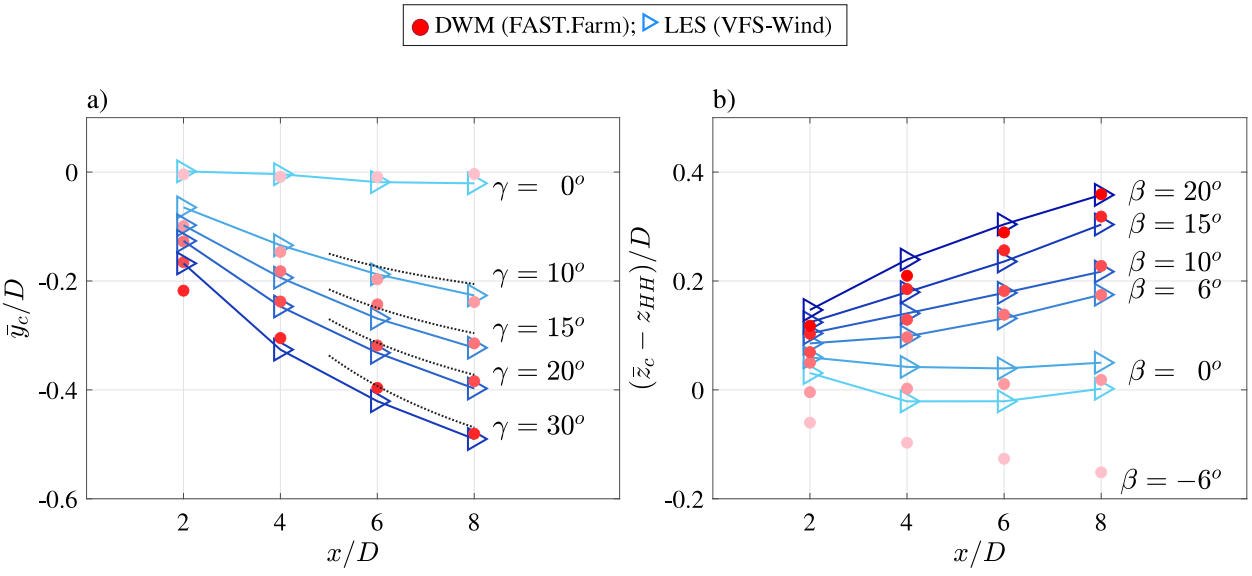

Fig. 14. Mean horizontal (a) and vertical (b) deflection of the wake, $\bar{y}_c$ and $\bar{z}_c$, at different downstream distances, for inflow 1, for every yaw and tilt case. For every case, the respective color is darker as γ or β increases. The red circles represent the DWM model estimation, and the triangles joined by the blue lines, the LES data. The C_{meand} used for each case and downstream location is fitted depending on the downstream distance x, see Table 7. The dotted lines represent the estimation of the wake deflection in yawed conditions by the analytical model from [12].

For the DWM model, two results with different C_{meand} filter sizes are compared to identify the influence of this parameter on the time series. The first value, $C_{\text{meand}} = 2.67$, is the one based on the work of Cheng and Porté-Agel [58]; the second value, $C_{\text{meand}} = 1.90$, is the default value suggested by FAST.Farm, based on Larsen et al. [19], and it is approximately the mean value of the filter used for cases 1a to 4a, i.e. the yaw misalignment cases. From both the time series (a) and the PSD (b), three main low frequency components at 0.0006, 0.0022 and 0.0050 Hz, outlined by vertical lines in the PSD, are captured by the two models, and the different levels of filtering. However, a strong dependence on the C_{meand} is found: the smallest filter, in red, presents a larger standard deviation and is therefore closer to the LES

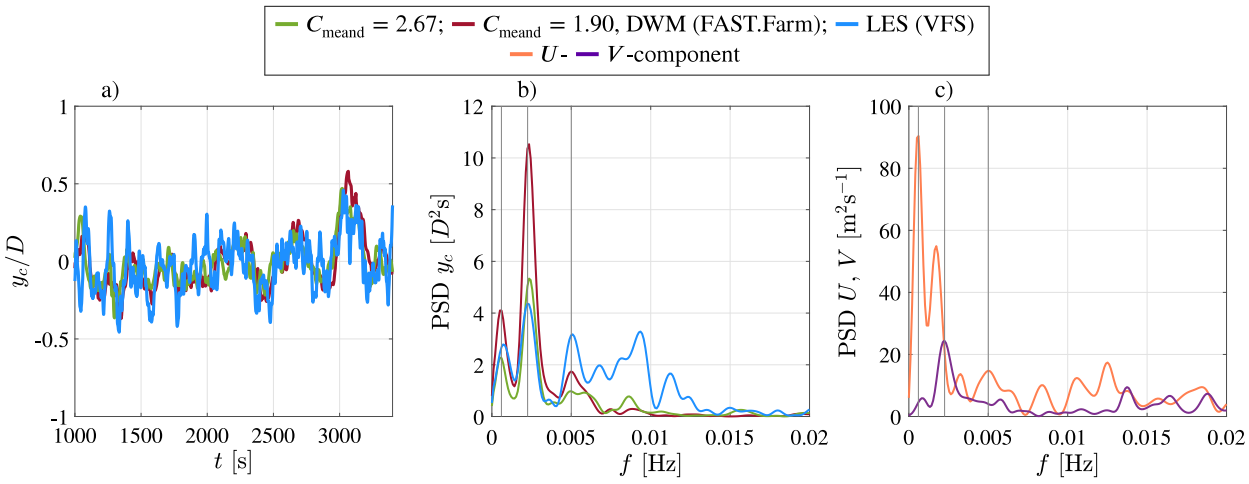

Fig. 15. Time series (a) and PSD (b) of the horizontal wake center meandering for $\gamma = 0°$, for the DWM model and two C_{meand} filters, and for LES, at $x = 8D$, for inflow 1; (c) PSD of the incoming wind speed U and V-components at the node at hub-height. The vertical lines indicate the frequencies f = 0.0006, 0.0022 and 0.005 Hz.

model. On the other hand, the higher energy content yielding this higher standard deviation is not at the same frequencies as the LES data, i.e. at $f \approx 0.01$ Hz. Instead, the energy content at 0.0006 and 0.0022 Hz is higher for this smaller filter. These higher energy content at these frequencies is also observed in the V-component (0.0022 Hz) and U-component (0.005 Hz) of the undisturbed incoming wind field in Fig. 15, (c). The main conclusion is that the lower frequencies, related to the U, V-components of the incoming wind field, are not only dominant in the meandering, but properly reproduced by the DWM model. However, higher frequency components, at approximately 0.01 Hz, are not captured by this model. This higher energy content identified in the LES data may be related to the shear-instability wake meandering mechanism, which has been characterized to fall in the range of a Strouhal's number, defined as $St = fD/U_{\infty,z_{HH}}$, between 0.1 and 0.5 [21]. In this case, St is equal to 0.27, and based on qualitative analyses of videos of the flow field, the hypothesis of this higher energy content being related to this mechanism is plausible.

The limitation inferred from these analyses is that even though the wake motion standard deviation is accurately reproduced by the DWM model if the polar grid size is properly adjusted, it tends to overestimate the energy in the lower frequency region, i.e. with a Strouhal's number lower than 0.1, and underestimates the wake oscillation induced by the shear-layer at higher frequencies.

Fig. 16 further investigates the effect of using the same polar grid size (C_{meand}) for the vertical wake meandering as for the horizontal one, for the case with $\gamma = \beta = 0°$. Consequently, the C_{meand} values used here are not the ones for the analyses in the previous sections related to the vertical wake misalignment. When comparing Figs. 15 and 16, it is clearly found that the motion amplitude predicted by the DWM model in the horizontal and vertical directions compares differently to LES when using the same filter size. The filter size, $C_{meand} = 1.90$ that yields a close result for the horizontal meandering in Fig. 15(a), heavily underestimates the vertical meandering in 16(a). This comparison implies that the filter size employed in the DWM model tuned in the horizontal direction does not automatically guarantee a close match in the vertical direction, but should be adjusted carefully.

Further insight into the time- and frequency-domain for yaw and tilt is given in the following. Fig. 17 shows the time series of the horizontal meandering of the wake center $y_c(t)$ and its PSD for $\gamma = 10°$ and $\gamma = 30°$, at $x = 8D$. The C_{meand} used in these cases are the ones corresponding to Table 2. The energy content related to the lower frequency range of the PSD is overestimated by the DWM model. As the frequency increases, it is underestimated, and the frequency signature at $f \approx 0.01$ Hz, presumably corresponding to a shear-layer-induced phenomenon, is absent from the DWM model prediction.

The vertical meandering for tilt deflection angles $\beta = 6°$ and 15°, depicted in Fig. 18, shows that the DWM model captures the lowest frequency with a higher energy content at 0.0006 Hz, related to the incoming wind field, for both cases. The higher frequency components, related to shear-layer instability meandering mechanisms, are not properly reproduced. This difference in the energy content is reflected in the standard deviation in Fig. 13, (d), as a general trend, and specifically for $\beta = 6°$ and 15°. In the DWM model, as the tilt angle increases from 6° to 15°, the energy content remains similar for the lowest frequency at 0.0006 Hz. However, in LES, the energy content decreases for this frequency as the tilt angle increases.

5.3. Available power in the wake

To further analyze the performance of the DWM model compared to LES data, we investigate the power available in the wake P_{wake}, at $x = 8D$. For the horizontal steering cases, the power is computed at the hub-plane, i.e. at $z = z_{HH}$, as the line integral of the available power per unit distance, i.e. $P_{wake} = \int_{-0.5D}^{0.5D} 0.5 \cdot \rho_{air} \cdot U^3_{y,z=z_{HH}} dy$; for the vertical steering cases, P_{wake} is computed at the center plane, i.e. at $y = 0$, as $P_{wake} = \int_{0.125D}^{1.125D} 0.5 \cdot \rho_{air} \cdot {U_{y=0,z}}^3 dz$. Fig. 19 presents the comparison of the available power output for the two models, at $x = 8D$, for inflow 1 and inflow 2. For the horizontal steering cases, the maximum difference between the models is 12%, for inflow 1, and for $\gamma = 15°$, for which the available power is underestimated by the DWM model. This underestimation is consistent with the larger time-averaged deficit, as presented in Fig. 8. For the vertical displacement cases, the difference between the models in the available power at the central plane is negligible.

6. Effect of the yaw and tilt wake steering on the power output of a waked turbine

Despite the limitations presented in the previous sections, the DWM model serves as a good compromise against LES to analyze the effect that yaw and tilt have on the power production, if the polar grid size of the model is adjusted accordingly. To estimate how the deflection of the wake may affect the power output of a wind turbine in the wake, the same set of cases was run in FAST.Farm, with a second IEA 15 MW wind turbine (T2) placed $8D$ downstream the first turbine in free wind (T1). T2 has an operating controller, i.e. not simplified to match the LES rotor configuration. Fig. 20 shows the increase in power output of T2 as the wake deflects due to the yaw misalignment or rotor tilt of the wind turbine in free wind. The results are normalized by the

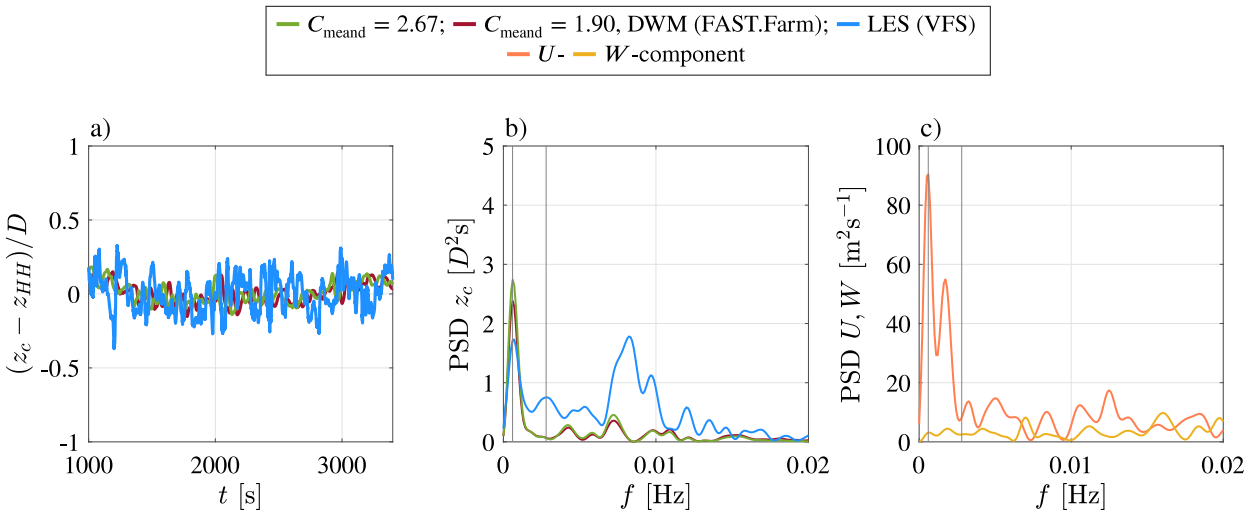

Fig. 16. Time series (a) and PSD (b) of the vertical wake center meandering for $\gamma = 0°$, for the DWM model and two C_{meand} filters, and for LES, at $x = 8D$, for inflow 1. PSD (c) of the incoming wind speed U and W-components at the node at hub-height z_{HH}. The vertical lines outline the frequencies f = 0.0006 and 0.0028 Hz.

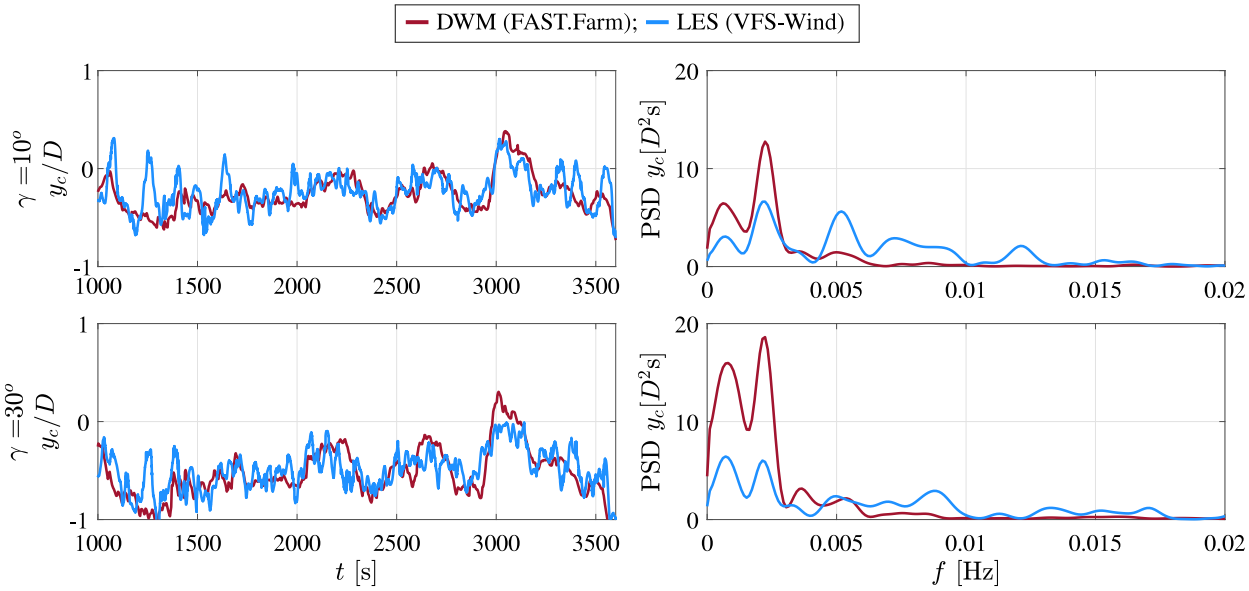

Fig. 17. Time series and PSD of the horizontal wake center meandering y_c at $x = 8D$, for the yaw misalignment cases with $\gamma = 10°$ and 30°, for inflow 1.

power output of T2 if T1 were not yawed or tilted ($P_{T2,\gamma=0}$ and $P_{T2,\beta=0}$, respectively). The power output of the turbine in the wake for $\gamma = 30°$ is almost doubled compared to completely waked conditions.

7. Conclusions

Wake steering strategies have gained significant attention from the academic and industry communities for reducing the adverse effects of wakes on downstream wind turbines in wind farms. Wake steering techniques intentionally create a misalignment between the rotor and the wind, effectively redirecting the wake in the lateral and/or vertical directions to mitigate the negative effects of wakes on power production and fatigue [8,11].

The present study aims to validate the dynamic wake meandering (DWM) model by comparing its predictions to large eddy simulation (LES) data, specifically focusing on its ability to predict the wake evolution under various horizontal and vertical wake steering strategies. The DWM model is widely used for analyzing the impact of wakes on power and loading, providing a unified framework [19,72]. The main research question addressed in this work is whether the current DWM model can accurately capture both the average wake deflection resulting from wake steering techniques (yaw or tilt) and the instantaneous oscillations (or meandering). The objective is to determine the extent to which the model can be applied to predict both the mean and dynamic wake effects under wake steering techniques. Additionally, we aim to identify any limitations that may guide future development.

To this end, two inflows with different shear and turbulence intensities and a mean wind speed of approximately 9 m/s are investigated with LES (VFS-Wind) and the DWM model (FAST.Farm). Twenty cases with yaw (γ) and tilt (β) misalignment are studied with the IEA 15 MW wind turbine. The focus is on the time-averaged velocity field and wake deficit downstream the wind turbine, the average wake deflection, vertical and horizontal, and the meandering, or standard deviation of the wake center displacement, at 8 rotor diameters (D) downstream. The main conclusions on the comparison of the results computed based on the DWM model, implemented in FAST.Farm, with the ones based on the high-fidelity LES results by VFS-Wind, include:

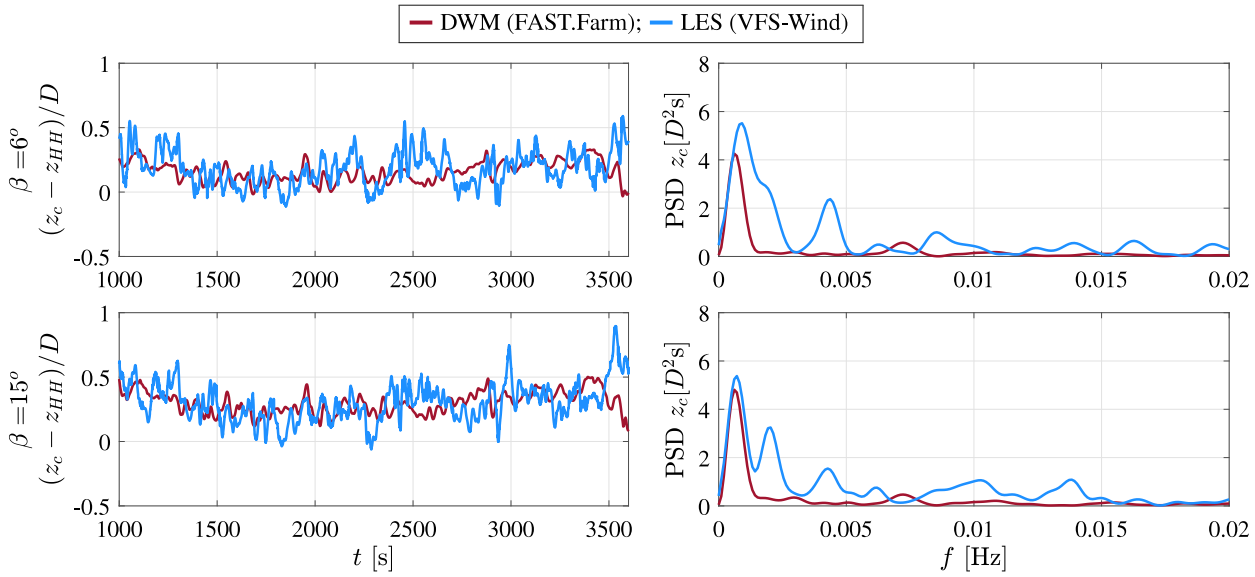

Fig. 18. Time series and PSD of the vertical wake center meandering z_c at $x = 8D$, for the tilt misalignment angles $\beta = 6°$ and 15°, for inflow 1.

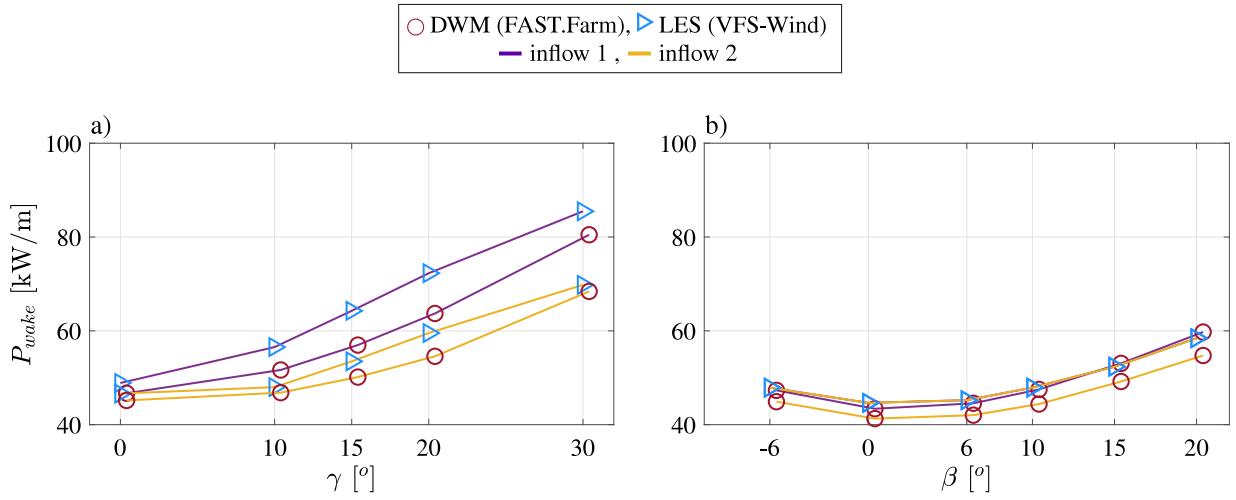

Fig. 19. Power available in the wake P_{wake} (a) at the hub-plane, in yawed conditions and (b) at the central plane at $y = 0$, for the tilted rotor conditions, at $x = 8D$, in LES and the DWM model, for both inflow 1 and 2.

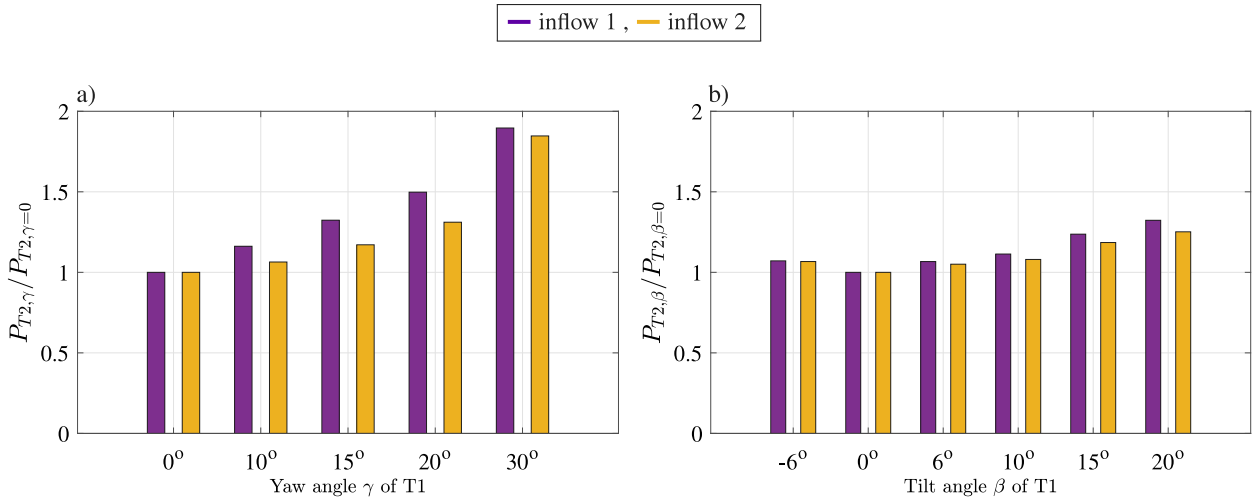

Fig. 20. Power output of the turbine in the wake $P_{T2,\gamma}$ (a) and $P_{T2,\beta}$ (b), for every case of yaw and tilt misalignment, respectively, and for the two turbulent inflows, inflow 1 and inflow 2. The power output is normalized by the power output of the same turbine (T2) if β and γ of the upstream turbine are zero ($P_{T2,\beta,\gamma=0}$).

- The mean and standard deviation of the horizontal and vertical meandering computed by the DWM model are sensitive to the filter size used to calculate the spatial-averaged velocity with which the wake planes are advected. As the polar grid area used to calculate this spatial-averaged velocity increases, the lower impact the deficit has on the averaged longitudinal component. This lower impact of the deficit leads to a smaller (V, W)-to-U ratio, and therefore to lower mean and standard deviation of the wake center meandering.
- If the filter size is appropriately selected, the horizontal wake steering in the DWM model, including the time-averaged wake deflection and velocity profiles, shows very similar results to the LES data for all the cases presented, and especially for $x \geq 6D$. The vertical wake steering shows very good agreement between the DWM model results to the LES data for cases with positive tilt angles ($\beta > 6°$). For $\beta \leq 0°$, discrepancies are observed when analyzing the mean value, mainly due to whether or not the presence of the ground is accounted for.
- Both the DWM model and LES approaches successfully capture the wake meandering induced by large eddies when the Strouhal's number (St) is less than 0.1. Furthermore, LES accurately captures the wake oscillation caused by the wake shear-layer when St is approximately 0.27. However, if the DWM model is tuned to accurately predict the wake center standard deviation, it tends to overestimate the amplitude of the motion in the lower frequency range.

The DWM model shows a generally good performance for the cases presented here. The main limitations of this tool as used in this work which affect the wake deficit and meandering are listed in the following. First, ground effects are not modeled, which has an impact mainly on the vertical wake steering. Second, the wake meandering frequencies related to shear-layer instability are not captured; these effects are observed at approximately 0.01 Hz, which coincides with the typical natural periods of floating wind turbines. Third, the nacelle and the tower are not accounted for in the wake deficit and meandering calculation. The last main limitation, based on the findings in this work, is related to the size of the polar grid used to calculate the spatial-averaged velocity with which the wake planes meander: this size cannot be adjusted for the vertical and horizontal deflection separately, which entails the limitation of not being able to, for instance, analyze a yaw-control strategy in floating wind farms, since fitting this size for a specific yaw angle will yield an overestimation of the mean vertical wake deflection. Additionally, the current DWM model implementation in FAST.Farm considers a fixed polar grid size in time and space in a given simulation, while the current results suggest that a streamwise variation might be useful.

Despite the limitations of the mid-fidelity tool, the DWM model provides a good compromise between its efficiency and accuracy, given the reduced computational cost: in the current case, FAST.Farm requires 3 h runtime to run 3600 s simulation on a single core, whereas VFS-Wind uses 48 h on 240 cores. By using the former, the power output gain of a wind turbine in the wake of the yawed and tilted rotors could be analyzed. From this analysis it was concluded that if the wind turbine in free-wind is yawed by $\gamma = 30°$, the power output of a turbine placed $8D$ downstream is almost doubled compared to if the turbine in free wind were not yawed.

Due to the computational cost constraints of LES, running the cases shown in this work to analyze the wake steering for other mean wind speed scenarios, and for more than one seed, was not feasible. However, future work should consider additional cases, and perform a similar analysis using the curled wake formulation of the DWM model.

CRediT authorship contribution statement

Irene Rivera-Arreba: Conceptualization, Methodology, Validation, Formal analysis, Investigation, Data curation, Writing – original draft, Writing – review & editing, Visualization, Project administration. **Zhaobin Li:** Conceptualization, Methodology, Software, Validation, Formal analysis, Investigation, Data curation, Writing – original draft, Writing – review & editing, Visualization, Project administration. **Xiaolei Yang:** Conceptualization, Methodology, Software, Resources, Writing – review & editing, Supervision, Project administration, Funding acquisition. **Erin E. Bachynski-Polić:** Conceptualization, Methodology, Resources, Writing – review & editing, Supervision, Project administration, Funding acquisition.

Declaration of competing interest

The authors declare the following financial interests/personal relationships which may be considered as potential competing interests: Xiaolei Yang reports financial support was provided by National Natural Science Foundation of China. Zhaobin Li reports financial support was provided by National Natural Science Foundation of China. Erin E. Bachynski-Polic reports financial support was provided by Research Council of Norway. Irene Rivera-Arreba reports financial support was provided by Research Council of Norway.

Acknowledgments

The research leading to these results has received funding from the Basic Science Center Program for "Multiscale Problems in Nonlinear Mechanics" of the National Natural Science Foundation of China (NO. 11988102), NSFC (NO. 12172360, NO.12202453), and by the Research Council of Norway through the ENERGIX programme (grant 294573) and industry partners Equinor, MacGregor, Inocean, APL Norway and RWE Renewables. The large eddy simulations were carried out on the ORISE Supercomputer.

Appendix. Influence of the tower on the wake deficit and meandering

As the DWM model in the present work does not include the tower's effect on the wake, we investigate how including this effect in the modeling affects the wake deficit and meandering by using LES. The modeling approach for the tower is similar to the immerse boundary method, with non-penetrating conditions enforced in the normal direction of the tower, and the frictional force in the tangential direction is computed with a wall modeled based on coefficients obtained from turbulent boundary layer experiments [34]. The analysis is based on three cases, i.e., zero yaw and tilt angle case ($\gamma = \beta = 0$), and yaw case ($\gamma = 30°$, $\beta = 0$) and tilt case ($\gamma = 0$, $\beta = 15°$), under inflow I1.

Fig. A.1 presents the instantaneous flow field. The main effect that can be inferred from this figure, if compared to Fig. 12, is the larger deficit at the near-wake region, due to the tower's effect. From the analysis in Fig. A.2, where the time-averaged velocity is presented for the same cases, $\gamma = \beta = 0°$, $\gamma = 30°$ and $\beta = 15°$, the decreasing effect of the tower on the time-averaged velocity deficit as the downstream distance increases is confirmed. Table A.1 retrieves the statistics of the vertical and horizontal meandering of the wake center, for the same cases, with and without the influence of the tower in the model. The largest effect is seen in the tilt deflection case ($\beta = 15°$), where there is a difference of 20% in the mean value. This difference in this case is expected, given the plane at which the wake approximately meanders vertically, i.e. at the plane xOz at $y = 0$, where the tower is expected to have the largest effect. Nevertheless, the statistics do not reveal a large effect of the tower on wake meandering.

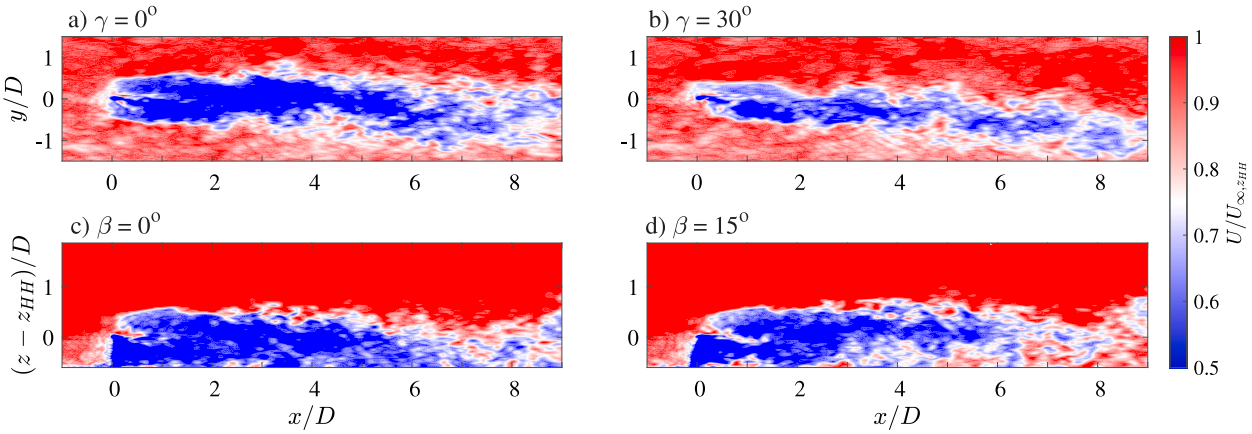

Fig. A.1. Instantaneous flow field for $\gamma = 0°$, and 30° and $\beta = 0°$ and 15°, for inflow 1 with the tower included; (a–b) streamwise velocity $U/U_{\infty,z_{HH}}$ at the hub-height plane xOy computed by LES; (c–d) streamwise velocity $U/U_{\infty,z_{HH}}$ at the xOz plane computed by LES.

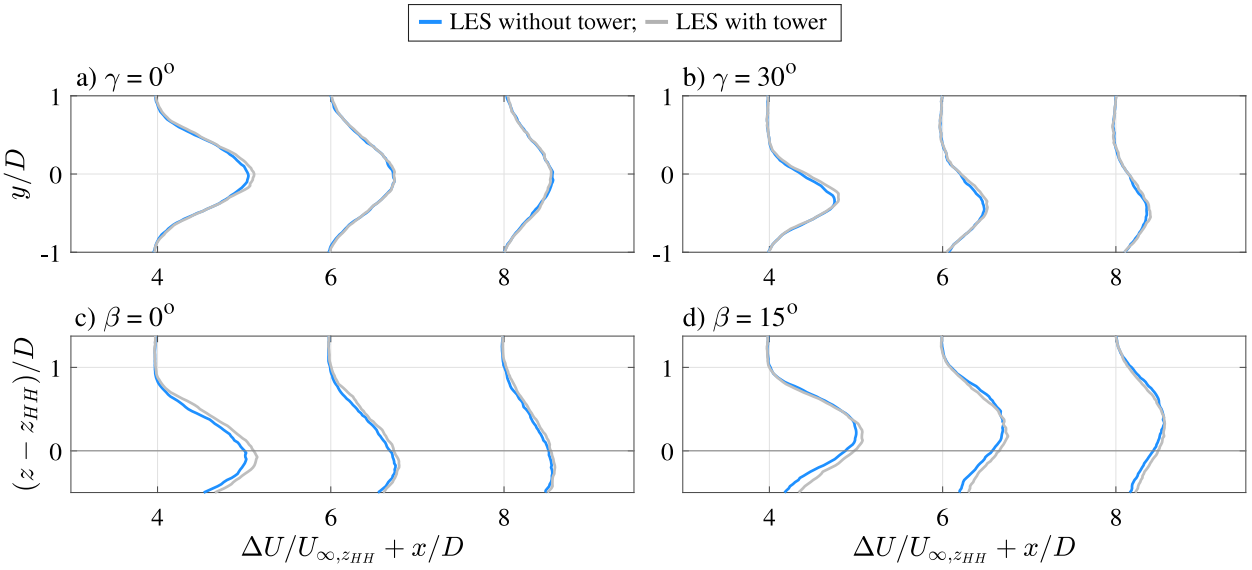

Fig. A.2. Effect of the tower on the time-averaged velocity deficit. (a, b) $\Delta U(y)/U_{\infty,z_{HH}}$, at $x = 4,\ 6$ and $8D$, at the hub-height plane for $\gamma = 0°$ and $\gamma = 30°$, for inflow 1; (c, d) $\Delta U(z)/U_{\infty,z_{HH}}$ at $x = 4,\ 6$ and $8D$, for $-0.5D < (z - z_{HH}) < 1.3D$, at the rotor plane for $\beta = 0°$ and $\beta = 15°$, for inflow 1. The hub-height in (c, d) is at $(z - z_{HH})/D = 0$, outlined by the solid horizontal line.

Table A.1
Effect of the tower on the wake statistics, the mean and the standard deviation, for $\gamma = \beta = 0°$ and $\gamma = 30°$ and $\beta = 0°$ and 15°, for inflow 1, at $x = 8D$.

Case	$\gamma = 0°$		$\beta = 0°$		$\gamma = 30°$		$\beta = 15°$	
Statistics [m]	$\bar{y}_c$	σ_{y_c}	$\bar{z}_c$	σ_{z_c}	$\bar{y}_c$	σ_{y_c}	$\bar{z}_c$	σ_{z_c}
Without tower	0.04	0.18	0.09	0.13	−0.41	0.20	0.30	0.15
With tower	0.03	0.19	0.00	0.11	−0.47	0.18	0.24	0.13

References

[1] R.J. Barthelmie, L.E. Jensen, Evaluation of wind farm efficiency and wind turbine wakes at the Nysted offshore wind farm, Wind Energy 13 (6) (2010) 573–586.

[2] R.J. Stevens, C. Meneveau, Flow structure and turbulence in wind farms, Annu. Rev. Fluid Mech. 49 (2017) 311–339.

[3] E. Simley, P. Fleming, J. King, Field validation of wake steering control with wind direction variability, J. Phys. Conf. Ser. 1452 (1) (2020) 012012.

[4] A.S. Wise, E.E. Bachynski, Wake meandering effects on floating wind turbines, Wind Energy 23 (5) (2019).

[5] E.M. Nanos, C.L. Bottasso, D.I. Manolas, V.A. Riziotis, Vertical wake deflection for floating wind turbines by differential ballast control, Wind Energy Sci. (2021).

[6] P. Doubrawa, S. Sirnivas, M. Godvik, Effects of upstream rotor tilt on a downstream floating wind turbine, J. Phys. Conf. Ser. 1934 (1) (2021) 012016.

[7] M. Bastankhah, F. Porté-Agel, Experimental and theoretical study of wind turbine wakes in yawed conditions, J. Fluid Mech. 806 (2016) 506–541.

[8] P. Fleming, P.M. Gebraad, S. Lee, J.-W. van Wingerden, K. Johnson, M. Churchfield, J. Michalakes, P. Spalart, P. Moriarty, Simulation comparison of wake mitigation control strategies for a two-turbine case, Wind Energy 18 (12) (2014) 2135–2143.

[9] M.F. Howland, J. Bossuyt, L.A. Martínez-Tossas, J. Meyers, C. Meneveau, Wake structure in actuator disk models of wind turbines in yaw under uniform inflow conditions, J. Renew. Sustain. Energy 8 (4) (2016) 043301.

[10] C.L. Archer, A. Vasel-Be-Hagh, Wake steering via yaw control in multi-turbine wind farms: recommendations based on large-eddy simulation, Sustain. Energy Technol. Assess. 33 (2019) 34–43.

[11] M.L. Aitken, R.M. Banta, Y.L. Pichugina, J.K. Lundquist, Quantifying wind turbine wake characteristics from scanning remote sensor data, J. Atmos. Ocean. Technol. 31 (4) (2014) 765–787.

[12] G.-W. Qian, T. Ishihara, A new analytical wake model for yawed wind turbines, Energies 11 (3) (2018) 665.

[13] M.F. Howland, J.B. Quesada, J.J.P. Martínez, F.P. Larrañaga, N. Yadav, J.S. Chawla, V. Sivaram, J.O. Dabiri, Collective wind farm operation based on a predictive model increases utility-scale energy production, Nat. Energy 7 (9) (2022) 818–827.

[14] P.A. Fleming, P.M. Gebraad, S. Lee, J.-W. van Wingerden, K. Johnson, M. Churchfield, J. Michalakes, P. Spalart, P. Moriarty, Evaluating techniques for redirecting turbine wakes using SOWFA, Renew. Energy 70 (2014) 211–218.

[15] J. Annoni, A. Scholbrock, M. Churchfield, P. Fleming, Evaluating tilt for wind plants, in: 2017 American Control Conference (ACC), IEEE, 2017, pp. 1–20.

[16] H.M. Johlas, D.P. Schmidt, M.A. Lackner, Large eddy simulations of curled wakes from tilted wind turbines, Renew. Energy 188 (2022) 349–360.

[17] C. Cossu, Replacing wakes with streaks in wind turbine arrays, Wind Energy 24 (4) (2020) 345–356.

[18] C. Cossu, Evaluation of tilt control for wind-turbine arrays in the atmospheric boundary layer, Wind Energy Sci. 6 (3) (2021) 663–675.

[19] G.C. Larsen, H.A. Madsen, K. Thomsen, T.J. Larsen, Wake meandering: a pragmatic approach, Wind Energy 11 (4) (2008) 377–395.

[20] X. Yang, F. Sotiropoulos, Wake characteristics of a utility-scale wind turbine under coherent inflow structures and different operating conditions, Phys. Rev. Fluids 4 (2019) 024604.

[21] M. Heisel, J. Hong, M. Guala, The spectral signature of wind turbine wake meandering: A wind tunnel and field-scale study, Wind Energy 21 (9) (2018) 715–731.

[22] M.J. Churchfield, S. Lee, P.J. Moriarty, Y. Hao, M.A. Lackner, R. Barthelmie, J.K. Lundquist, G. Oxley, A comparison of the Dynamic Wake Meandering model, Large-Eddy Simulation, and field data at the Egmond aan Zee offshore wind plant, in: 33rd Wind Energy Symposium, American Institute of Aeronautics and Astronautics, 2015, pp. 1–20.

[23] J. Jonkman, P. Doubrawa, N. Hamilton, J. Annoni, P. Fleming, Validation of FAST. farm against large-eddy simulations, J. Phys. Conf. Ser. 1037 (2018) 062005.

[24] E. Gaertner, J. Rinker, L. Sethuraman, F. Zahle, B. Anderson, G. Barter, N. Abbas, F. Meng, P. Bortolotti, W. Skrzypinski, G. Scott, R. Feil, H. Bredmose, K. Dykes, M. Shields, C. Allen, A. Viselli, IEA Wind TCP Task 37: Definition of the IEA 15-Megawatt Offshore Reference Wind Turbine, Technical Report, NREL, 2020.

[25] A. Calderer, X. Yang, D. Angelidis, A. Khosronejad, T. Le, S. Kang, A. Gilmanov, L. Ge, I. Borazjani, Virtual flow simulator, 2015, URL: https://www.osti.gov/biblio/1312901.

[26] X. Yang, F. Sotiropoulos, R.J. Conzemius, J.N. Wachtler, M.B. Strong, Large-eddy simulation of turbulent flow past wind turbines/farms: the Virtual Wind Simulator (VWiS), Wind Energy 18 (12) (2015) 2025–2045.

[27] D. Foti, Coherent vorticity dynamics and dissipation in a utility-scale wind turbine wake with uniform inflow, Theor. Appl. Mech. Lett. 11 (5) (2021) 100292.

[28] Z. Li, X. Yang, Large-eddy simulation on the similarity between wakes of wind turbines with different yaw angles, J. Fluid Mech. 921 (2021).

[29] Z. Li, G. Dong, X. Yang, Onset of wake meandering for a floating offshore wind turbine under side-to-side motion, J. Fluid Mech. 934 (2022) A29.

[30] X. Yang, M. Pakula, F. Sotiropoulos, Large-eddy simulation of a utility-scale wind farm in complex terrain, Appl. Energy 229 (2018) 767–777.

[31] Z. Wang, G. Dong, Z. Li, X. Yang, Statistics of wind farm wakes for different layouts and ground roughness, Bound.-Lay. Meteorol. (2023) 1–36.

[32] Y. Zhang, Z. Li, X. Liu, F. Sotiropoulos, X. Yang, Turbulence in waked wind turbine wakes: Similarity and empirical formulae, Renew. Energy 209 (2023) 27–41.

[33] J. Smagorinsky, General circulation experiments with the primitive equations: I. the basic experiment, Mon. Weather Rev. 91 (3) (1963) 99–164.

[34] X. Yang, F. Sotiropoulos, A new class of actuator surface models for wind turbines, Wind Energy 21 (5) (2018) 285–302.

[35] D.A. Knoll, D.E. Keyes, Jacobian-free Newton–Krylov methods: a survey of approaches and applications, J. Comput. Phys. 193 (2) (2004) 357–397.

[36] Y. Saad, A flexible inner-outer preconditioned GMRES algorithm, SIAM J. Sci. Comput. 14 (2) (1993) 461–469.

[37] L. Ge, F. Sotiropoulos, A numerical method for solving the 3D unsteady incompressible Navier–Stokes equations in curvilinear domains with complex immersed boundaries, J. Comput. Phys. 225 (2) (2007) 1782–1809.

[38] Z. Li, X. Liu, X. Yang, Review of turbine parameterization models for large-eddy simulation of wind turbine wakes, Energies 15 (18) (2022) 6533.

[39] A. Jimenez, A. Crespo, E. Migoya, J. García, Advances in large-eddy simulation of a wind turbine wake, in: Journal of Physics: Conference Series, Vol. 75, IOP Publishing, 2007, 012041.

[40] J.N. Sorensen, W.Z. Shen, Numerical modeling of wind turbine wakes, J. Fluids Eng. 124 (2) (2002) 393–399.

[41] W.Z. Shen, J.H. Zhang, J.N. Sørensen, The actuator surface model: a new Navier-Stokes based model for rotor computations, J. Solar Energy Eng. (2009).

[42] J. Wang, C. Wang, F. Campagnolo, C.L. Bottasso, Wake behavior and control: comparison of LES simulations and wind tunnel measurements, Wind Energy Sci. 4 (1) (2019) 71–88.

[43] R.J. Stevens, L.A. Martínez-Tossas, C. Meneveau, Comparison of wind farm large eddy simulations using actuator disk and actuator line models with wind tunnel experiments, Renew. Energy 116 (2018) 470–478.

[44] N. Troldborg, F. Zahle, P.-E. Réthoré, N. Sorensen, Comparison of the wake of different types of wind turbine CFD models, in: 50th AIAA Aerospace Sciences Meeting Including the New Horizons Forum and Aerospace Exposition, 2012, p. 237.

[45] G. Dong, Z. Li, J. Qin, X. Yang, Predictive capability of actuator disk models for wakes of different wind turbine designs, Renew. Energy 188 (2022) 269–281.

[46] S.-P. Breton, C.S. Watters, C. Masson, S. Gomez-Iradi, X. Munduate, On the prediction of tip vortices in the near wake of the MEXICO rotor using the actuator surface method, Int. J. Eng. Syst. Model. Simul. 46 4 (1–2) (2012) 11–26.

[47] K. Nilsson, W.Z. Shen, J.N. Sørensen, S.-P. Breton, S. Ivanell, Validation of the actuator line method using near wake measurements of the MEXICO rotor, Wind Energy 18 (3) (2015) 499–514.

[48] X. Yang, J. Hong, M. Barone, F. Sotiropoulos, Coherent dynamics in the rotor tip shear layer of utility-scale wind turbines, J. Fluid Mech. 804 (2016) 90–115.

[49] J. Hong, M. Toloui, L.P. Chamorro, M. Guala, K. Howard, S. Riley, J. Tucker, F. Sotiropoulos, Natural snowfall reveals large-scale flow structures in the wake of a 2.5-MW wind turbine, Nat. Commun. 5 (1) (2014) 4216.

[50] L.P. Chamorro, R.E. Arndt, F. Sotiropoulos, Reynolds number dependence of turbulence statistics in the wake of wind turbines, Wind Energy 15 (5) (2012) 733–742.

[51] J. Jonkman, K. Shaler, FAST.Farm User's Guide and Theory Manual, NREL, Boulder, Colorado, 2021.

[52] National Renewable Energy Laboratory (NREL), OpenFAST 3.4.0, 2023, https://github.com/OpenFAST/openfast.

[53] H.A. Madsen, G.C. Larsen, T.J. Larsen, N. Troldborg, R. Mikkelsen, Calibration and validation of the Dynamic Wake Meandering model for implementation in an aeroelastic code, J. Solar Energy Eng. 132 (4) (2010).

[54] R.E. Keck, A Consistent Turbulence Formulation for the Dynamic Wake Meandering Model in the Atmospheric Boundary Layer (Ph.D. thesis), DTU, Denmark, 2013.

[55] P. Doubrawa, J.R. Annoni, J.M. Jonkman, Optimization-based calibration of FAST. Farm parameters against Large-Eddy Simulations, in: 2018 Wind Energy Symposium, American Institute of Aeronautics and Astronautics, 2018, pp. 1–20.

[56] E. Branlard, L.A. Martínez-Tossas, J. Jonkman, A time-varying formulation of the curled wake model within the FAST.Farm framework, Wind Energy (2022).

[57] S. Øye, Dynamic stall simulated as time lag of separation, in: Proceedings of the Fourth IEA Symposium on the Aerodynamics of Wind Turbines, 1990.

[58] W.-C. Cheng, F. Porté-Agel, A simple physically-based model for wind-turbine wake growth in a turbulent boundary layer, Bound.-Lay. Meteorol. 169 (1) (2018) 1–10.

[59] P. Brugger, C. Markfort, F. Porté-Agel, Field measurements of wake meandering at a utility-scale wind turbine with nacelle-mounted Doppler lidars, Wind Energy Sci. 7 (1) (2022) 185–199.

[60] Z. Du, M. Selig, A 3-D stall-delay model for horizontal axis wind turbine performance prediction, in: 1998 ASME Wind Energy Symposium, 1998, p. 21.

[61] W.Z. Shen, R. Mikkelsen, J.N. Sørensen, C. Bak, Tip loss corrections for wind turbine computations, Wind Energy 8 (4) (2005) 457–475.

[62] H. Glauert, Airplane propellers, in: Aerodynamic Theory, Springer Berlin Heidelberg, 1935, pp. 169–360.

[63] T. Burton, N. Jenkins, D. Sharpe, E. Bossanyi, Wind Energy Handbook, Wiley, 2011.

[64] P.Å. Krogstad, J. Lund, An experimental and numerical study of the performance of a model turbine, Wind Energy 15 (3) (2011) 443–457.

[65] J. Bartl, Experimental Testing of Wind Turbine Wake Control Methods (Ph.D. thesis), NTNU, 2018.

[66] B. Blocken, T. Stathopoulos, J. Carmeliet, CFD simulation of the atmospheric boundary layer: wall function problems, Atmos. Environ. 41 (2) (2007) 238–252.

[67] G. Wang, X. Zheng, Very large scale motions in the atmospheric surface layer: a field investigation, J. Fluid Mech. 802 (2016) 464–489.

[68] H. Liu, G. Wang, X. Zheng, Three-dimensional representation of large-scale structures based on observations in atmospheric surface layers, J. Geophys. Res.: Atmos. 124 (20) (2019) 10753–10771.

[69] J.S. Irwin, A theoretical variation of the wind profile power-law exponent as a function of surface roughness and stability, Atmos. Environ. (1967) 13 (1) (1979) 191–194.

[70] S. Emeis, Current issues in wind energy meteorology, Meteorol. Appl. 21 (4) (2014) 803–819.

[71] D. As, DNV-RP-C205: Environmental Conditions and Environmental Loads, Veritas Offshore Technology and Service AS, Oslo, 2019.

[72] IEC, IEC61400-1: Wind Energy Generation Systems– Part 1: Design Requirements, Technical Report, IEC, Geneva, Switzerland, 2019.

[73] WMO, Guide To Meteorological Instruments and Methods of Observation, World Meteorological Organization, 2008.

[74] K. Shaler, J. Jonkman, N. Hamilton, Effects of inflow spatiotemporal discretization on wake meandering and turbine structural response using FAST.Farm, J. Phys. Conf. Ser. 1256 (2019) 012023.

[75] T. Guo, X. Guo, Z. Gao, S. Li, X. Zheng, X. Gao, R. Li, T. Wang, Y. Li, D. Li, Nacelle and tower effect on a stand-alone wind turbine energy output—A discussion on field measurements of a small wind turbine, Appl. Energy 303 (2021) 117590.

[76] G.D. Cillis, S. Cherubini, O. Semeraro, S. Leonardi, P.D. Palma, POD-based analysis of a wind turbine wake under the influence of tower and nacelle, Wind Energy 24 (6) (2020) 609–633.
[77] Z. Gao, Y. Li, T. Wang, W. Shen, X. Zheng, S. Pröbsting, D. Li, R. Li, Modelling the nacelle wake of a horizontal-axis wind turbine under different yaw conditions, Renew. Energy 172 (2021) 263–275.
[78] C. Santoni, K. Carrasquillo, I. Arenas-Navarro, S. Leonardi, Effect of tower and nacelle on the flow past a wind turbine, Wind Energy 20 (12) (2017) 1927–1939.
[79] F. Porté-Agel, M. Bastankhah, S. Shamsoddin, Wind-turbine and wind-farm flows: A review, Bound.-Layer Meteorol. 174 (1) (2020) 1–59.
[80] X. Yang, F. Sotiropoulos, A review on the meandering of wind turbine wakes, Energies 12 (24) (2019) 4725.
[81] P. Brugger, M. Debnath, A. Scholbrock, P. Fleming, P. Moriarty, E. Simley, D. Jager, J. Roadman, M. Murphy, H. Zong, et al., Lidar measurements of yawed-wind-turbine wakes: characterization and validation of analytical models, Wind Energy Sci. 5 (4) (2020) 1253–1272.